Master's Thesis

A 150 MHz all sky survey with the Precision Array to Probe the Epoch of Reionization

Author:
James Kariuki Chege

Supervisors:
Prof. Gianni Bernardi
Prof. Oleg Smirnov
Dr. Chuneeta D. Nunhokee

A thesis submitted in fulfilment of the requirements for the degree of Master of Science

in Physics

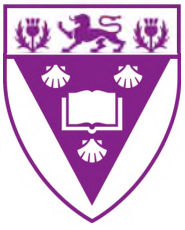

RHODES UNIVERSITY
Where leaders learn

Centre for Radio Astronomy Techniques and Technologies
Department of Physics and Electronics

June 4, 2019

Abstract

The Precision Array to Probe the Epoch of Reionization (PAPER) was built to measure the redshifted 21 cm line of hydrogen from cosmic reionization. Such low frequency observations promise to be the best means of understanding the cosmic dawn; when the first galaxies in the universe formed, and also the Epoch of Reionization; when the intergalactic medium changed from neutral to ionized. The major challenges to these observations is the presence of astrophysical foregrounds that are much brighter than the cosmological signal.

Here, I present an all-sky survey at 150 MHz obtained from the analysis of 300 hours of PAPER observations. Particular focus is given to the calibration and imaging techniques that need to deal with the wide field of view of a non-tracking instrument. The survey covers ~ 7000 square degrees of the southern sky.

From a sky area of 4400 square degrees out of the total survey area, I extract a catalogue of sources brighter than 4 Jy whose accuracy was tested against the published GLEAM catalogue, leading to a fractional difference rms better than 20%.

The catalogue provides an all-sky accurate model of the extragalactic foreground to be used for the calibration of future Epoch of Reionization observations and to be subtracted from the PAPER observations themselves in order to mitigate the foreground contamination.

Acknowledgements

To all those without which there is no way (not even in my dreams), I would have managed to do this work.

Foremost, I am deeply grateful to Oleg for allowing me to pursue this level of education at RATT using the NRF/SKA bursary. I also hereby thank NRF/SKA. I am greatly indebted to my Supervisor, Gianni for his guidance throughout this masters. His deep insight and emphasis on thoroughly understanding every concept has definitely made me a better student. He not only initiated me into the the world of astronomy research, but he also did it well. I also thank Ridhima for her great assistance in development and application of python scripts for this work. Ronel Groenwald made all the administration work look easy and to that I am very grateful. To all my RATT colleagues in Grahamstown who became family; Alex, Cyndie, Diana, Eric, Gift, Kela, Kwazi, Lexy, Siyanda, Sam and Ulrich. Thank you for the much help to my work, the stimulating discussions, the memorable fun moments and the constructive debates.

Apart from academia, I express much gratitude to my family, especially my mom, dad and sisters for their moral support and constant calls. Mom, Your prayers always work and your son is soaring high! Special thanks goes to Jemimah Wambui. Though you were miles away all this time, your shoulder was close enough to lean on. We did it!

Finally, and most importantly, I wish to express my gratitude to the almighty God for his grace and providence throughout the 2 years of study.

To my mom, Priscillah Njoki Chege, for all the sacrifices you made for Wangari, Njeri, and I.

Declaration of Authorship

I, James Chege, declare that this thesis titled, '*A 150 MHz all sky survey with the Precision Array to Probe the Epoch of Reionization*' and the work presented in it are my own. I confirm that:

- This work was done wholly or mainly while in candidature for a research degree at this University.
- Where any part of this thesis has previously been submitted for a degree or any other qualification at this University or any other institution, this has been clearly stated.
- Where I have consulted the published work of others, this is always clearly attributed.
- Where I have quoted from the work of others, the source is always given. With the exception of such quotations, this thesis is entirely my own work.
- I have acknowledged all main sources of help.
- Where the thesis is based on work done by myself jointly with others, I have made clear exactly what was done by others and what I have contributed myself.

Signed: _____

Date: _____

Contents

Chapter 1

Introduction

In the last few decades, astronomers have made huge leaps towards a better understanding of the universe. Using instruments such as the Hubble Space Telescope, they have been able to observe galaxies as far back as a billion years after the Big Bang. Furthermore, observations of the Cosmic Microwave Background (CMB, Hinshaw et al., 2013; Planck Collaboration et al., 2016) give us a glimpse of how the primordial universe looked. This has led to the development and general acceptance of the 6-parameter Lambda Cold Dark Matter (ΛCDM) as the current concordance model of the universe.

The evolution of the universe during its first billion years, from the fluctuations imprinted in the CMB to the birth of the galaxies remains largely unobserved. The study of the underlying processes behind the period when there were no luminous objects ('dark ages') to the formation of the very first stars and galaxies which lit up the universe is a major avenue of research in modern cosmology. This thesis, which uses radio interferometric observations, revolves around this era, coming in as one piece of the many required to complete a well understood early universe.

1.1 The Big Bang and thereafter

In this section, I give a brief overview of the history of the universe highlighting only the major events relevant to the occurrence of cosmic reionisation.

Our universe is believed to have expanded from a singularity. After 10^{-36} seconds it underwent a phase of rapid expansion known as inflation (Guth, 1981; Linde, 1982). After inflation, the universe contained a hot and dense fluid where photons and baryons were tightly coupled together via Thomson scattering of photons by electrons (Carroll & Ostlie, 2007). Thomson scattering made the universe opaque to radiation as

photons could not travel long distances. The universe remained opaque until it was $\sim$ 380000 years old ($z \approx 1370$[1]), when matter and radiation decoupled and the CMB photons essentially free streamed until they reach us today. At this epoch, the universe temperature dropped to $T \approx 3700$ K, allowing for electrons and protons to recombine into neutral Hydrogen (HI).

Recombination represents the last scattering between matter and photons, imprinted in the CMB fluctuations (Penzias & Wilson, 1965; Dicke et al., 1965; Mather et al., 1994; Bennett et al., 2013; Adam et al., 2016).

The next era that followed the last scattering, is usually referred to as the dark ages. This period witnessed the growth of matter fluctuations under the action of gravity.

1.1.1 The Epoch of Reionization

As the dark ages progressed, clumps of neutral Hydrogen continued to grow until those that are within dark matter haloes above a certain critical mass eventually collapsed under their self gravity, igniting to form the first stars and galaxies (Abel et al., 2002; Bromm & Larson, 2004; Frebel et al., 2007; Loeb, 2010). These first stars likely formed at $z \approx 30$, when the universe was roughly one million years old, terminating the dark ages. As star formation progressed in these early galaxies, ultra-violet radiation eventually escaped the host galaxies, starting the ionization of the surrounding intergalactic medium (IGM). Such Epoch of Reionization (EoR, Figure 1.1) has been the subject of intense theoretical studies, although it remains a largely unknown process.

In the next section, I summarise different observational probes used as evidence of cosmic reionization.

1.2 Observational evidence for reionisation

1.2.1 High-redshift quasars

Quasars are used as reionization probes as the intervening neutral Hydrogen absorbs their ultraviolet radiation. In particular, neutral Hydrogen is opaque to Lyα radiation and, if the intergalactic medium is neutral between the quasar and the observer, one expects to see an absorption profile in the quasar spectrum bluewards of the Lyα in

[1]More details on the timelines for recombination and last scattering mentioned here can be found in Ryden Barbara's 'Introduction to Cosmology' book (Ryden, 2013).

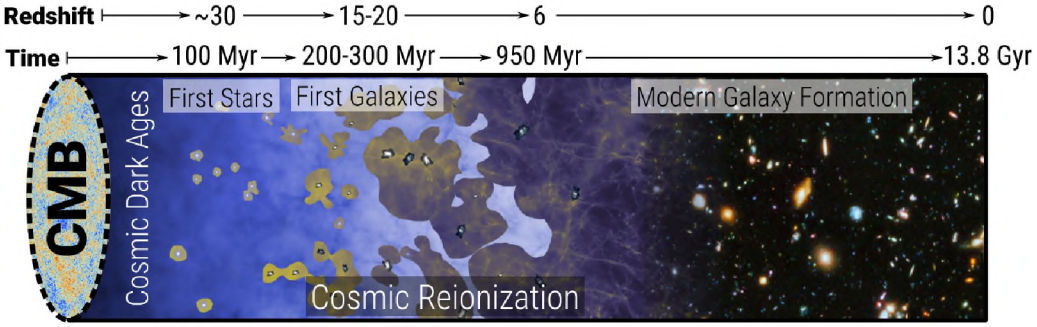

FIGURE 1.1: Picture illustrating the transition from neutral IGM left after the universe recombined at $z \approx 1100$ to the fully ionised IGM observed today. After recombination, when the CMB observed today as photons from the last scattering surface were released, hydrogen in the IGM remained neutral until the first stars and galaxies formed at $z \approx 30$. The galaxies released energetic UV photons capable of ionising local bubbles of hydrogen gas. As the abundance of these early galaxies increased, the bubbles increasingly overlapped and progressively larger volumes became ionised. The reionization process completed at $z \approx 6$, approximately 1 Gyr after the Big Bang. Image credit: J. Wise, Caltech.

the quasar rest frame. This effect is known as the Gunn-Peterson effect (GP, Gunn & Peterson, 1965).

Observations of 19 quasars in the $5.74 \leq z \leq 6.42$ range showed an accelerated increase in the GP optical depth with z, higher than what would be caused by just density evolution (Fan et al., 2006). Several quasars at $z > 6$ showed a complete GP absorption, indicating that the Hydrogen neutral fraction should have risen above 0.1 (Fan et al., 2006). These observations provide evidence that reionization was likely complete by $z \simeq 6$.

Quasar absorption spectra completely saturate when the GP optical depth is greater than ~ 0.1. The GP trough can only be useful in placing lower limits on the GP optical depth and HI neutral fraction thus constraining the ending stages of EoR (Becker et al., 2015; Mortlock, 2016).

1.2.2 Galaxy surveys and Lyα emitting galaxies

Galaxy surveys are important probes for cosmic reionisation. To this end, there have been two complementary methods used to both identify new galaxies at high redshifts and also determine their contribution towards reionisation. The first is the Lyman-break drop-out technique, that takes advantage of the absorption trough (flux density "drop-out") blueward of the 912 Å Lyman limit (e.g., Mclure et al., 2011; Bouwens et al., 2015). The second is the observation of the luminosity function of galaxies with bright Lyα emission (Lyα emitters, Malhotra & Rhoads, 2004; Ouchi et al., 2010).

The fraction of Lyman-break galaxies has been observed to increase from $z \approx 2$ to $z \approx 6$ followed by a sudden decrease at $z \approx 7$ onwards with even a further decrease at $z \approx 8$ (Caruana et al., 2012; Treu et al., 2013). This has been explained by the increase of the hydrogen neutral fraction, $x_{\rm HI}$, up to $x_{\rm HI} \approx 0.5$ at $z \approx 7$ (e.g., Dijkstra et al., 2011; Jensen et al., 2013).

The luminosity function of Lyα emitters shows very little evolution in the $3 < z \lesssim 6.5$ range, consistent with an IGM that is highly ionized at redshifts $z \lesssim 6.5$ (e.g., Malhotra & Rhoads, 2004; Kashikawa et al., 2006). The number of Lyα emitters also decreases significantly at $6 < z < 7$ indicating an increase in the neutral part of the IGM (Fan et al., 2006; Hu et al., 2010). Both methods therefore seem to indicate a significant increase in the neutral Hydrogen fraction at $z > 6.5$ (e.g., Dijkstra & Wyithe, 2012).

These two methods are consistent with each other, having independently shown that the observed Lyα flux from galaxies at $z > 6$ is suppressed significantly when compared to extrapolations from lower redshift data (e.g., Dijkstra & Wyithe, 2012).

1.2.3 CMB polarization

Thomson scattering between free electrons in the ionized intergalactic medium with the local CMB quadrupole anisotropies damps the primary temperature anisotropies while also producing linear polarization at the horizon scale (Zaldarriaga, 1997; Hu & White, 1997). This signal appears as a bump in the E–mode CMB power spectrum whose amplitude is proportional to the optical depth of the intergalactic medium τ, which is given by the line of sight integral of the free electrons density n_e:

$$\tau = \int_0^{z_{\rm reion}} \sigma_T \, n_{{\rm e}(z)} \, dl \tag{1.1}$$

where σ_T is the Thomson cross-section and $H(z)$ is the Hubble parameter. Current measurements of the CMB optical depth suggest that, if reionization occured instantaneously and ended at $z \sim 6$ as indicated by quasar absorption spectra, it happened at $z \approx 8.8$ (Planck Collaboration et al., 2016; Adam et al., 2016).

There are also several secondary probes of reionisation that can be obtained from CMB measurements. An example, which can be used as a probe of patchy reionisation is the kinetic Sunyaev-Zeldovich (kSZ) effect. The kSZ effect occurs when scattered CMB photons are doppler shifted due to the bulk velocity of free electrons relative to the CMB. Small scale variations in the ionization fraction during the EoR lead to a patchy kSZ signal (Aghanim et al., 2008). The signal amplitude depends on the duration of

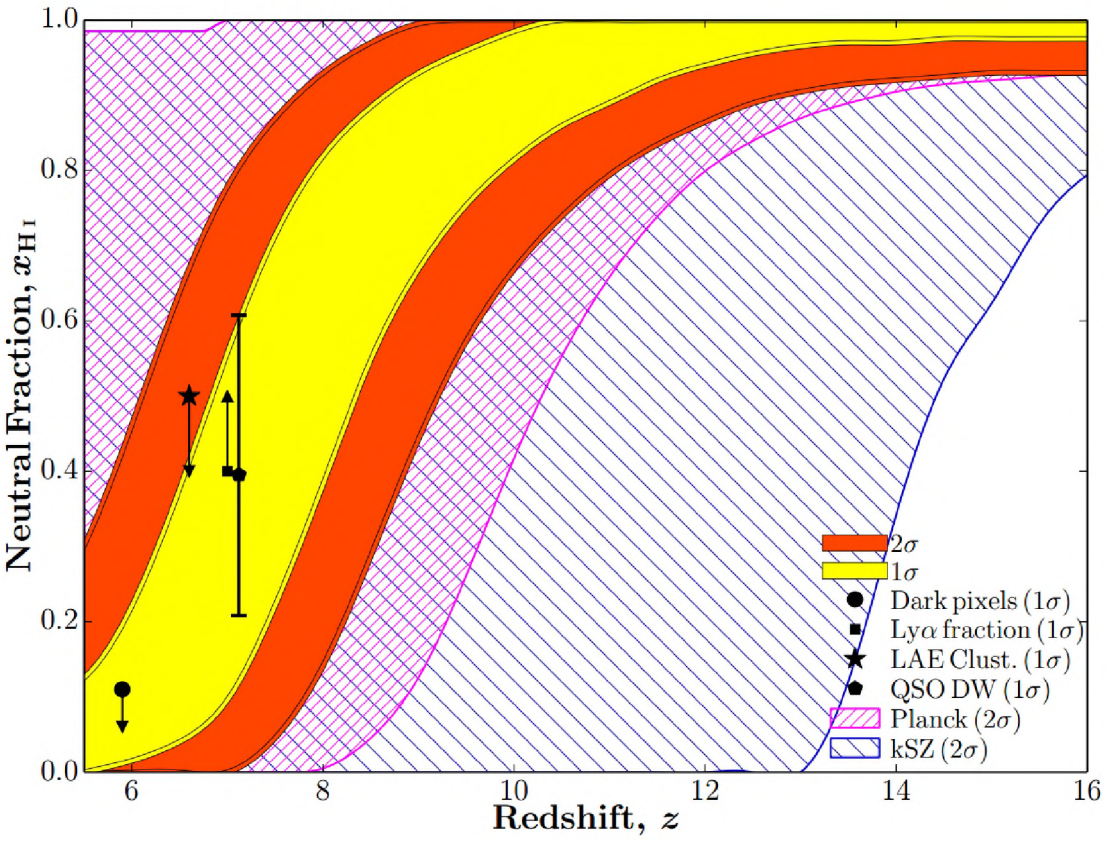

FIGURE 1.2: The evolution of the IGM neutral fraction. Observations include the dark pixel fraction in quasar spectra, the CMB optical depth, the evolution of the fraction Lyα emitters, LAE clustering and the patchy kSZ (Greig & Mesinger, 2017).

reionization, while its shape depends on the distribution of ionized bubble sizes (Reichardt, 2016). Zahn et al. (2012) used measurements of the patchy kSZ to constrain the duration of reionization to be $\Delta z \leq 4.4$. A similar study by George et al. (2014) gave consistent results obtaining an upper limit of $\Delta z < 5.4$ at the 95% confidence level.

1.2.4 Current constraints on the evolution of the IGM neutral fraction

Despite our incomplete knowledge of cosmic reionization, Greig & Mesinger (2017) jointly analysed the available observations to draw the most up to date picture of the evolution of the IGM neutral fraction (Figure 1.2). Although the 2σ uncertainties allow for a broad range of histories with an extended beginning of reionization when the neutral fraction $x_{\rm HI}$ is larger than 90%, the joint analysis favours a reionization history whose midpoint is $z \approx 7.6$ and a duration $\Delta z \sim 1-2$ (defined between the redshift at which $x_{\rm HI} = 0.25$ and $x_{\rm HI} = 0.75$).

1.3 The 21 cm line as a probe of cosmic reionisation

The alternative way to observe the dark ages and EoR is the use of the neutral Hydrogen hyperfine transition line that occurs at a rest wavelength of 21 cm. Since neutral Hydrogen was the most abundant element in the universe throughout the dark ages up to the middle phases of the EoR, the 21 cm line can thus be used as a direct tracer of the HI evolution.

The 21 cm line originates from the spin flip between the two fundamental states of the neutral Hydrogen atom (Figure 1.3). The energy difference between the two states is $\Delta E = 5.9 \times 10^{-6}$ eV and thus the emitted photon has a frequency of 1420 MHz which corresponds to a 21 cm wavelength (Van de Hulst, 1945; Ewen. & Purcell., 1951). If emitted by a high redshift cloud, 21 cm emission undergoes a $(1 + z)$ redshift stretch to the metre-wavelengths regime for $z > 6$.

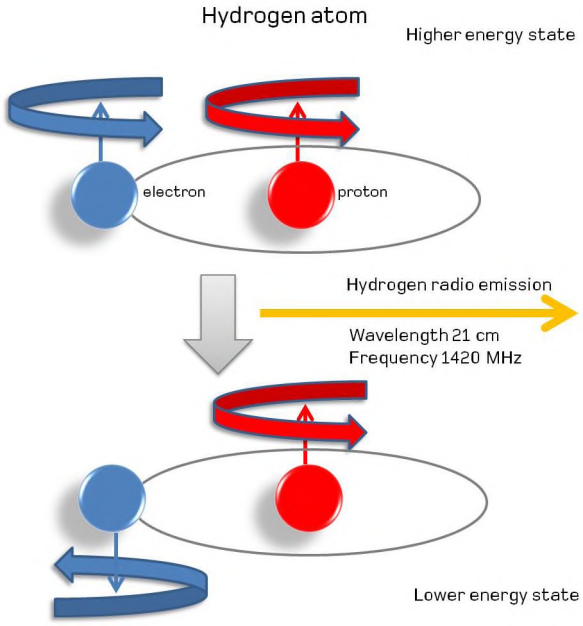

FIGURE 1.3: The emission of the 21 cm line due to a flip in the energy state of a neutral hydrogen atom. Image credit: SKA Organisation.

The expression for the differential 21 cm brightness temperature, $\delta T_{\rm b} \equiv T_{\rm b} - T_{\rm CMB}$, which gives the fluctuations of $T_{\rm b}$ with respect to the the CMB temperature ($T_{\rm CMB}$), is given by (e.g., Furlanetto et al., 2006; Zaroubi, 2013; Mesinger et al., 2015):

$$\delta T_{\rm b} = 28(1+\delta)x_{\rm HI}\left(1 - \frac{T_{\rm CMB}}{T_{\rm s}}\right)\left(\frac{\Omega_{\rm b}h^2}{0.0223}\right)\sqrt{\left(\frac{1+z}{10}\right)\left(\frac{0.24}{\Omega_m}\right)}\left[\frac{H(z)/(1+z)}{d\nu_{\parallel}/dr_{\parallel}}\right] \text{mK}, \tag{1.2}$$

where Ω_m and Ω_b are the mass and baryon densities in units of the critical density, δ denotes the density contrast, h is the Hubble constant, $\frac{d\nu_{\parallel}}{dr_{\parallel}}$ represents the gradient of

the proper velocity along the line of sight which includes both the Hubble expansion and the peculiar velocity (Kaiser, 1987; Furlanetto & Furlanetto, 2007). $T_{\rm s}$ is the spin temperature which represents the excitation energy of the 21 cm line. It can be described by using the Boltzmann distribution to examine the relative population of HI atoms in the two hyperfine states:

$$\frac{n_1}{n_0} = \frac{g_1}{g_0} e^{-\frac{\Delta E}{k_B T_{\rm s}}} = 3e^{\frac{-0.068K}{T_{\rm s}}}, \tag{1.3}$$

where n_1, n_0 represent the density of atoms in the two hyperfine levels and g_1, g_0 are the statistical weights ($\frac{g_1}{g_0} = 3$). k_B is the Boltzmann's constant and $\Delta E = 5.9 \times 10^{-6}$ eV. The spin temperature can therefore be defined as the value that defines the relative abundance of hydrogen atoms in the higher and lower energy ground states (Furlanetto et al., 2006).

The 21 cm signal is therefore only observable if $T_{\rm s}$ is different from the background temperature. The absorption of CMB photons would naturally lead $T_{\rm s}$ to an equilibrium with the CMB temperature, and thus making the 21 cm line unobservable. There are two main mechanisms that can drive the spin temperature away from the CMB temperature and couple it (even if partially) to the gas temperature, T_k, which is the other factor involved:

- Collisional coupling: collisions between hydrogen atoms can induce a spin flip. Collisions are effective only in the early stages when the gas density is high;
- The Wouthuysen-Field effect (Wouthuysen, 1952; Field, 1959): UV radiation from higher redshift sources is doppler shifted to the Lyα line at lower redshifts. An HI atom can absorb a Lyα photon exciting it into a higher level. This is followed by a spontaneous decay which returns the atom into either of the two ground hyperfine levels with a possible change of spin state (see Figure 1.4).

Figure 1.5 shows the redshift evolution of the three temperatures $T_{\rm CMB}$, $T_{\rm k}$ and $T_{\rm s}$ as a function of z. At $z \gtrsim 200$ the gas temperature is coupled to the CMB temperature through Compton scattering off of residual electrons left after recombination (Furlanetto et al., 2006). At $z \approx 200$ the fraction of ionized gas has decreased to less than 10^{-3} making Compton scattering inefficient: The gas and the CMB gradually decouple and the gas cools adiabatically faster than the CMB.

In this model, the first luminous objects are formed at $z \approx 30$ and they start heating up the gas. $T_{\rm s}$ is coupled to $T_{\rm k}$ at $z \gtrsim 100$ due to collisional coupling until $z \approx 80$ when this process becomes inefficient due to the cosmic expansion. $T_{\rm s}$ then approaches $T_{\rm CMB}$ and is eventually coupled to it.

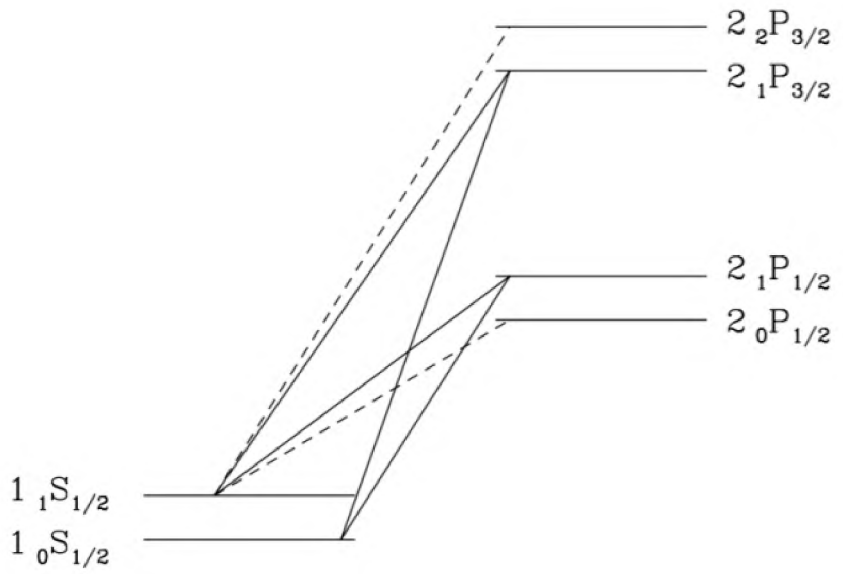

FIGURE 1.4: The Wouthuysen-Field effect schematic diagram. Solid (dashed) lines indicate possible (forbidden) transitions. Through the absorption of a Lyα photon a HI atom can be excited into either of the central 2P levels followed by a de-excitation which might result into a different spin state from the initial one and, therefore, re-emit a 21 cm photon (Furlanetto et al., 2006).

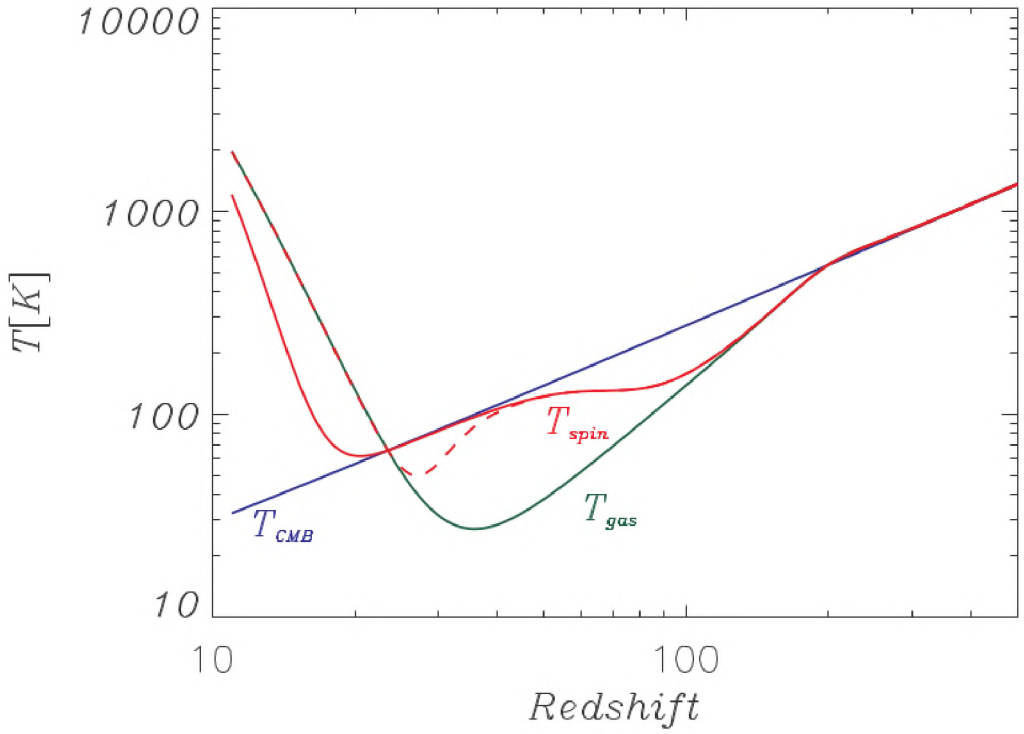

FIGURE 1.5: The redshift evolution of the CMB (blue line), gas (green line) and the spin (solid and dashed red line) temperature respectively (Zaroubi, 2013).

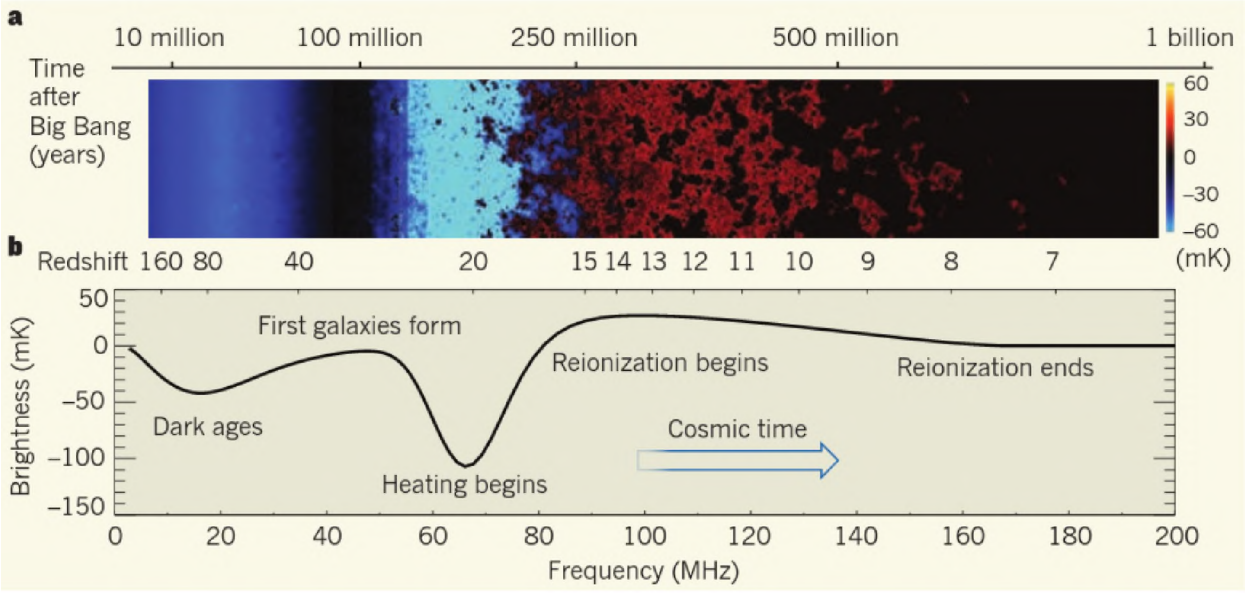

FIGURE 1.6: Evolution of the 21 cm signal as a function of redshift (frequency). Upper: Spatial fluctuations of the 21 cm signal. Lower: Sky-averaged 21 cm signal (Mellema et al., 2006; Pritchard & Loeb, 2012).

At $z \sim 30$ the formation of the first stars couples the spin temperature to the gas temperature via the WF effect. The WF effect essentially couples the spin temperature to the temperature corresponding to the UV background, also referred to as "colour" temperature, which is, in turn, coupled to the kinetic gas temperature due to the high optical deth of Lyα scattering, bringing the gas and the radiation field into local equilibrium (Pritchard & Loeb, 2012). Gas heating begins at $z \sim 20$ quickly driving the gas temperature above the CMB temperature ($10 < z < 20$), ultimately up to hundreds of Kelvin degrees. When the $T_s = T_k \gg T_{\rm CMB}$, the spin temperature does not affect the IGM evolution significantly anymore.

Next we describe how the redshift evolution of these three temperatures affects the expected 21 cm brightness temperature (Figure 1.6, with the bottom panel showing the sky-averaged brightness temperature). At $z < 80$, after the gas decoupled from the CMB, the 21 cm signal is seen in absorption against the CMB. Fluctuations in the 21 cm signal are driven by matter density which follows dark matter fluctuations (Barkana & Loeb, 2001). At $z \sim 30$, when the WF coupling occurs, 21 cm signal can still be seen in absorption. The depth of the absorption trough is reached when the gas starts to be heated and depends upon the heating sources: Hard X-ray binaries or miniquasars lead to a rapid heating, whereas soft X-ray sources heat the gas less efficiently and lead to a a deeper and wider trough (Pritchard & Loeb, 2012).

After the gas was heated well above the CMB, the ionization fraction is the main driver of the 21 cm brightenss temperature. At $z \approx 6$, most of the HI is ionized and the 21 cm

signal disappears.

1.4 Fluctuations of the 21 cm line

In the previous sections, we have discussed the global 21 cm signal. However, this one-dimensional signal does not capture information on how the 21 cm brightness temperature evolves spatially. Spatial fluctations in the 21 cm signal are often described statistically through the 21 cm power spectrum $P(k)$ (e.g., Furlanetto et al., 2006; Morales et al., 2006):

$$\langle T_b(\vec{k})\tilde{T}_b(\vec{k'})\rangle = (2\pi)^3\delta(x)(k-k')P(k), \tag{1.4}$$

where k is the Fourier conjugate of x, $\langle\rangle$ indicates the ensemble average and δ is the Dirac delta function.

An example of the evolution of the 21 cm power spectrum is shown in Figure 1.7, alongside with slices from a numerical simulation (Mesinger et al., 2011). The general evolution is qualitatively similar in most models, however, the exact timing and duration of the different periods is model dependent and may change significantly.

The first row shows the simulation slice and power spectrum at $z \approx 30$. The only significant 21 cm emission is localized around the brightest galaxies as their ultraviolet emission couples the spin to the gas temperature via the Wouthuysen-Field effect. As the gas is colder than the CMB, the isolated pockets of 21 cm signal are seen in absorption against the CMB and can even reach to values of $\delta T_b < -100$ mK. Fluctuations in the spin temperature therefore trace the distribution of ultraviolet sources and are the main contribution to the power spectrum. The spin temperature gets more strongly coupled to the gas temperature until WF coupling saturates and at this point the spin temperature gets to its minimum value.

The second row at $z \approx 21$ is the onset of X-ray heating from the first sources, likely accreting stellar black holes. Here, the spin temperature has been fully coupled to the gas temperature throughout the whole simulation volume that therefore shows significant 21 cm signal everywhere. As most of the gas is still colder than the CMB, the majority of the 21 cm signal is in absorption against the CMB. Around the brightest sources where the 21 cm signal was in absorption at $z \approx 30$, it is now seen in emission, as the gas has been heated above the CMB by the radiation emitted by the sources. The power spectrum is now mostly driven by the fluctuations in the gas temperature and its amplitude, due to the large contrast between cold and hot gas regions, is one order of magnitude larger than at $z \approx 30$.

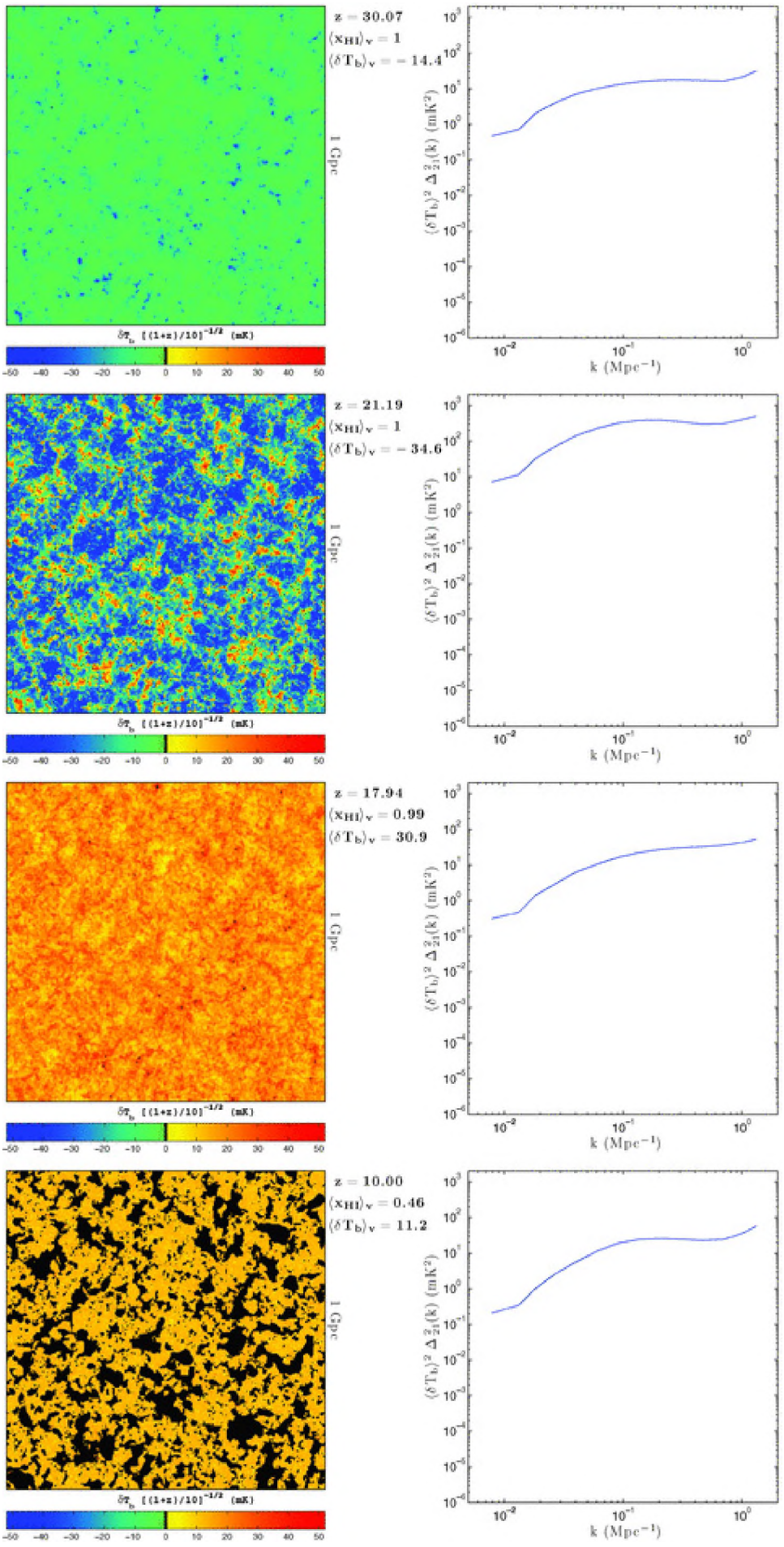

FIGURE 1.7: Slices from a semi-numerical simulation of the 21 cm signal featuring δT_b at $z = 30.1$, 21.1, 17.9 and 10. The slices are 1 Gpc wide and 3.3 Mpc deep (Mesinger et al., 2011).

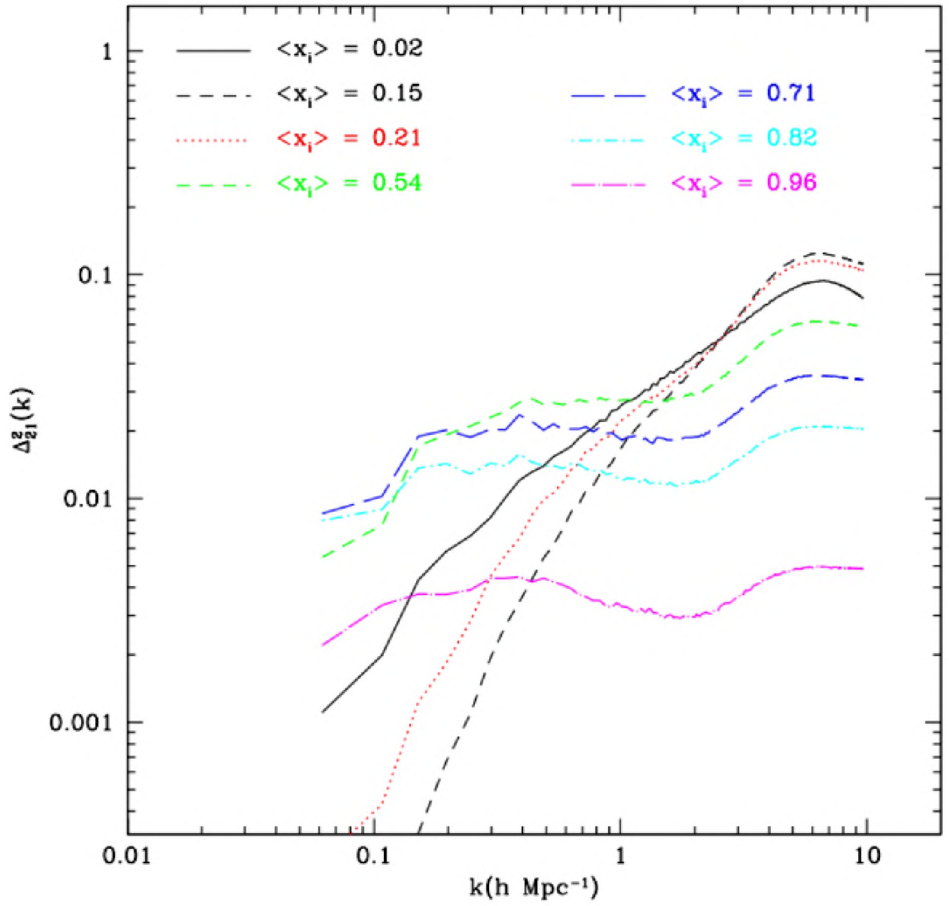

FIGURE 1.8: Power spectrum of the 21 cm signal brightness temperature over mean ionisation fraction values within the range $\langle x_i \rangle \in (0, 1)$ and redshift values within $z \in (11.46, 6.77)$. See text below for details. Image from (Lidz et al., 2008).

The third row at $z \approx 18$ shows an IGM heated to saturation, i.e. $T_{\rm s} \gg T_{\rm CMB}$, across the whole cosmic volume. This is a result of X-rays permeating from sources to almost all parts of the IGM. From this moment onward, the 21 cm brightness temperature becomes essentially independent of the spin temperature. The gas is still almost completely neutral, apart from small regions around the brightest sources. The 21 cm signal is however now in emission, and at a maximum before reionisation begins in earnest. As the IGM has been heated rather uniformly, fluctuations depend now essentially on the density field whose amplitude is smaller than the gas temperature fluctuations.

The fourth row shows the $z \approx 10$ slice when reionisation is well underway, i.e. when the average ionization fraction is $\sim 50\%$. The dark patches represent the ionised gas and are surrounded by neutral gas with a temperature $T_k \gg 100$ K. Ionizing photons have traversed resulting in patches of ionized gas and in those patches, the 21 cm signal disappears. The power spectrum shape and amplitude are driven by the morphology of the ionized regions while contributions from inhomogenous X-ray heating and Lyα coupling to the power spectrum are negligible (Santos et al., 2008).

Figure 1.8 shows the evolution of the dimensionless power spectrum given by $\Delta^2_{21}(k) = k^3 P_{21}(k)/(2\pi^2)$ throughout cosmic reionization for a series of mean ionization fraction ($\langle x_i \rangle$), with the assumption that $T_{\rm s} \gg T_{\rm CMB}$ (Lidz et al., 2008).

Initially, when $\langle x_i \rangle < 0.5$, the IGM is neutral and ionized bubbles are yet to establish any significant effect. The power spectrum thus follows the matter power spectrum. The power then decreases on the large scales because the ionised regions appear first on the densest regions (e.g., Iliev et al., 2006; Lidz et al., 2008). At $\langle x_i \rangle \approx 0.5$ the contrast between the ionised bubbles and the neutral gas around them dominates the maps causing the power to increase on the large scales and peaking at the characteristic scale of the ionised bubbles (e.g., McQuinn et al., 2007). On scales smaller than the ionised bubbles, the 21 cm power spectrum is smaller than the expected matter power spectrum resulting in an overall flattening of $\Delta^2_{21}(k)$ throughout reionisation. The power spectrum amplitude gradually decreases with increasing $\langle x_i \rangle > 0.5$ (Mellema et al., 2006).

1.5 Current status of EoR observations

The 21 cm signal has been elusive to observations so far. A new generation of radio interferometers operating at frequencies below 200 MHz was deployed over the last two decades in attempts to measure the 21 cm signal from cosmic reionization. It includes the Murchison Widefield Array (MWA, Tingay et al., 2013; Bowman et al., 2013), the Low Frequency Array (LOFAR, van Haarlem et al., 2013), the Precision Array for Probing the Epoch of Reionization (PAPER, Parsons et al., 2010) and the Hydrogen Epoch of Reionization Array (HERA, Deboer et al., 2017). These experiments are aimed at observing fluctuations in the redshifted 21 cm line. Figure 1.9 displays a compilation of the most recent upper limits from the various telescopes. Current measurements are still a couple of orders of magnitude away from constraining expected 21 cm models.

There have also been experiments designed to detect the sky-averaged/global 21 cm brightness temperature. They include the Experiment to Detect the Global EoR Signature (EDGES, Bowman & Rogers, 2010), Large Aperture Experiment to Detect the Dark Ages (LEDA, Price et al., 2018) among others. Recently, EDGES has reported a detection of the 21 cm global signal from the cosmic dawn. They presented the measurement of an absorption profile centred at 78 MHz ($z \approx 17$) with a 0.5 K amplitude (Figure 1.10). The EDGES signal has sparked a vigorous debate in the community as their 21 cm signal is twice as bright as the most optimistic literature model, implying that the gas temperature during this epoch must be significantly colder than predicted in any conventional cosmological model. Barkana (2018) attempted to explain the extra-cooling through non-gravitational interactions of the gas with the dark matter.

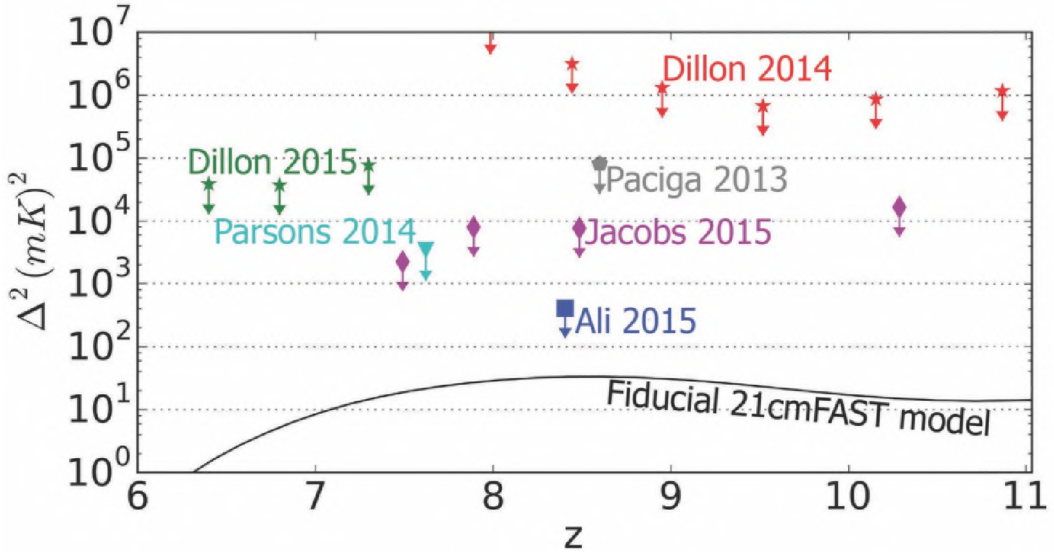

FIGURE 1.9: Current upper limits on the 21 cm power spectrum (Deboer et al., 2017).

Hills et al. (2018) re-analyzed the Bowman et al. (2018) data and raised concerns with the original analysis, in particular they indicated that the foreground model used by Bowman et al. (2018) is questionable as it may lead to some best fit parameter whose values are unphysical. Independent confirmations of the EDGES result are still awaited.

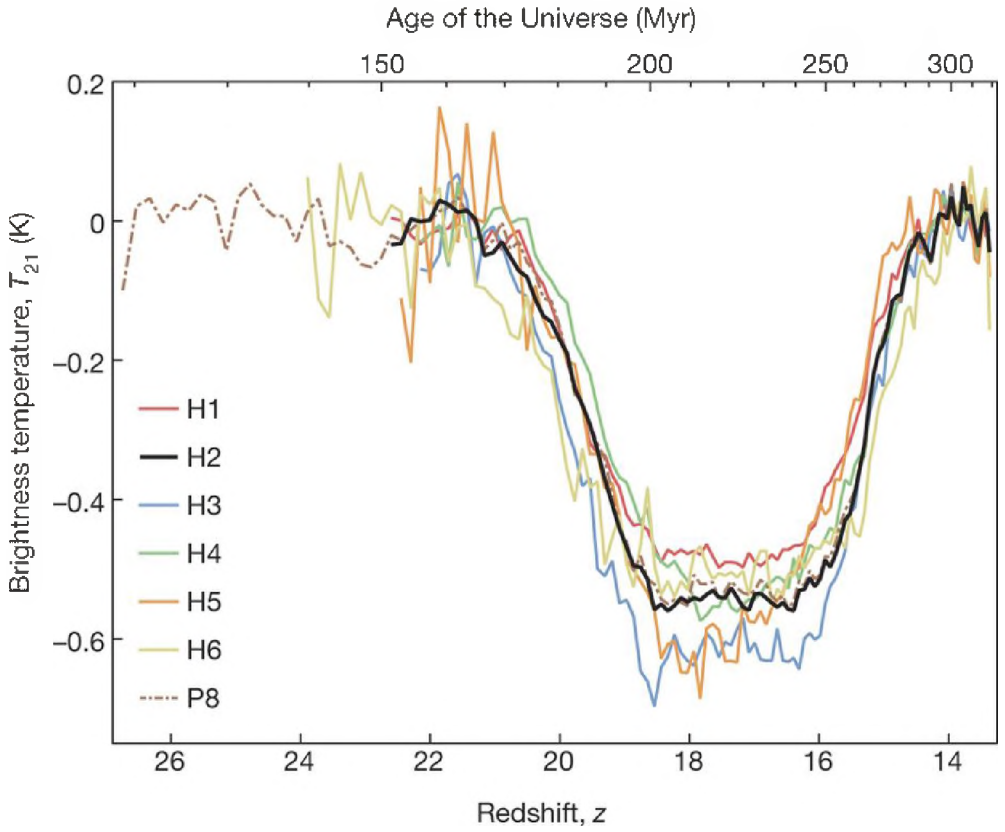

FIGURE 1.10: The 21 cm absorption profile detected by the EDGES collaboration (Bowman et al., 2018). Different colour lines indicate different experimental configurations.

Chapter 2

Challenges in EoR observations

There are several challenges to observations of the cosmological 21 cm signal. Low radio frequencies are often contaminated by radio frequency interference (RFI). These frequencies are heavily used by the FM radio band and satellite communication channels which also lie within this range. To minimise this contamination to the data, EoR arrays are constructed in remote areas, as far as possible from excessive human activity.

The ionosphere is no longer transparent at frequencies below 200 MHz. It is constituted of ionized plasmas whose electron column density changes with time, leading to time-variable refraction and scattering of the celestial radio waves that are observed by the interferometer as differential delays between signal reaching two different receptors, eventually leading to displacement of celestial sources (e.g., Jordan et al., 2017) and, in the most severe cases, to their scintillation and distortion (Loi et al., 2015; Mevius et al., 2016).

The most significant challenge to EoR observations is, however, the contamination by bright, unwanted foregrounds of Galactic and extragalactic origin (Morales & Hewitt, 2004; Wang et al., 2006; Bernardi et al., 2009; Liu et al., 2009). In attempts to minimise these foregrounds, usually the first obvious step is to restrict observations to areas of the sky where foregrounds are minimal such as high galactic latitude portions away from the galactic plane and prominent point sources (Bernardi et al., 2009; Procopio et al., 2017; Pindor, 2018). That alone is however not sufficient, owing to the faintness of the 21 cm signal that has a brightness temperature of few mK on a few arcmin angular scales while the foregrounds are estimated to be a few orders of magnitude brighter (Shaver et al., 1999; Morales & Hewitt, 2004; Wang et al., 2006; Bernardi et al., 2009). The success of EoR experiments is therefore heavily reliant on how well we understand and are able to characterise these astrophysical foregrounds.

In this chapter, I give an overview of foregrounds, including their different types, and the various methods developed for tackling them.

2.1 Galactic synchrotron emission

Galactic synchrotron emission is the dominant form of EoR foregrounds, accounting for 70% of the radio sky signal. It originates from the interaction between relativistic electrons in the interstellar medium and magnetic fields. Generally, relativistic electrons emit radiation, beamed in the direction of motion, at the critical frequency, ν_c (e.g., Longair, 2011),

$$\nu_c = \frac{\gamma^2 eB}{2\pi m_e}, \tag{2.1}$$

where γ is the Lorentz factor, e the electron charge, B is the magnetic field strength and m_e is the electron mass. The synchrotron spectrum S from an ensemble of electrons emitting at different ν_c spans a wide frequency range and is close to a featureless power law (Rybicki & Lightman, 1986):

$$S \propto \nu^{-\beta}, \tag{2.2}$$

where β is the spectral index (Longair, 2011).

The 408 MHz all-sky map by Haslam et al. (1982) is still the most accurate template of the Galactic synchrotron emission at frequencies below 1 GHz (Figure 2.1). Synchrotron emission is higher in the Galactic plane and decreases with Galactic latitude, although not in a uniform way but showing several spatial features like spurs and shells. The Galactic 408 MHz emission can be explained as the sum of two components: emission from the Galactic plane (thick disk) and the Galactic halo (thin disk, Beuermann et al., 1985).

The Galactic synchrotron spectral index β varies significantly across the sky, indicating the presence of different populations of relativistic electrons. Platania et al. (2003) found an average spectral index between 408 and 2326 MHz of $\langle\beta\rangle = -2.70$ with a $\sigma_\beta = 0.12$ dispersion.

Measurements at lower frequencies have been mostly carried out with single dipoles, therefore obtaining information averaged over spatial scales of tens of degrees. In the $100 - 200$ MHz range, the synchrotron spectral index lies in the $2.3 < \beta < 2.62$ range (Rogers & Bowman, 2008; Patra et al., 2015; Mozdzen et al., 2017). Mozdzen et al. (2017) found little variation across the 180° of their survey, i.e. $2.60 < \beta < 2.62$. The

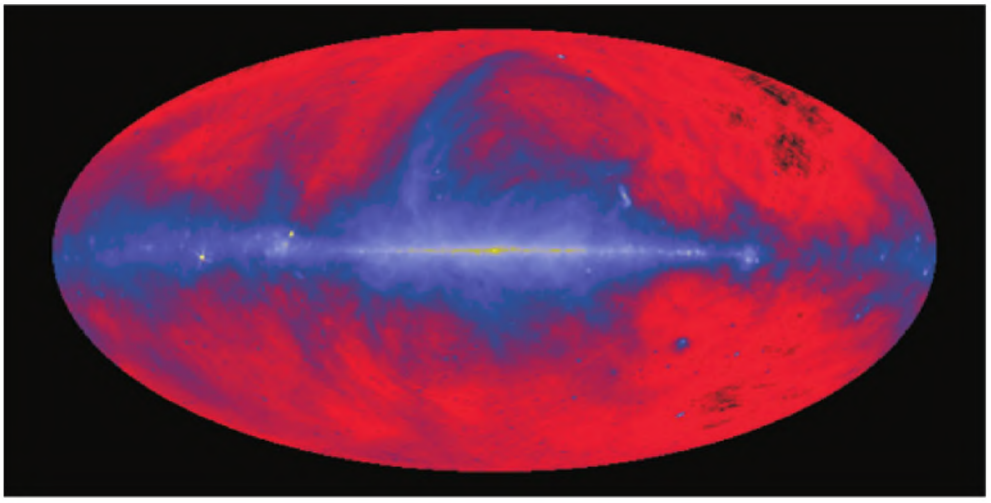

FIGURE 2.1: The 408 MHz all-sky map (Haslam et al., 1982). Image courtesy of Max-Planck Institute for Radio Astronomy, Bonn.

same area was surveyed at $50 - 100$ MHz by Mozdzen et al. (2018) and they found a slight flattening of the spectral index $2.54 < \beta < 2.59$.

Synchrotron emission is intrinsically polarized (Rybicki & Lightman, 1986). Diffuse Galactic emission shows prominent polarization down to $\sim$ 300 MHz (e.g., Wieringa et al., 1993; Haverkorn et al., 2003a,b). Observations over the last decade have started to characterize the properties of Galactic polarization in the $100 - 200$ MHz range too. In selected patches at high Galactic latitude, fluctuations in the Galactic polarized foreground on arcminutes scales are fainter than 1 K (Pen et al., 2009; Bernardi et al., 2009), but can become as bright as $\sim$ 13 K closer to the Galactic plane (Bernardi et al., 2009).

The most comprehensive polarization survey at high Galactic latitude was carried out by Bernardi et al. (2013), covering $\sim$ 2400 square degrees. It shows significant variations across the sky with fluctuations ranging from a few hundreds mK up to $\sim$ 13 K.

2.2 Extragalactic foregrounds

Extragalactic radiation is emitted by radio sources especially hosting an active galactic nucleus (AGN). AGNs emit via the synchrotron mechanism due to the accretion of gas around supermassive black holes located at the centre of the galaxy.

Several surveys at low radio frequencies were carried out over the last few decades. The Westerbork Northern Sky Survey (Rengelink et al., 1997) covered the whole sky north of declination $\delta = +30°$ at 325 MHz with arcmin resolution, detecting sources down to

a flux density of 18 mJy. At even lower frequencies, the 6C survey (Hales et al., 1988) at 151 MHz and the Very Large Array Low-frequency Sky Survey at 74 MHz (Cohen et al., 2004) provided the best description of the extragalactic radio sky.

Recent improvements have come with the new low frequency arrays. The LOFAR collaboration has started the Million Source Sky Survey by observing a $100° \times 100°$ area in the $30 - 160$ MHz range, with a $\approx 20''$ angular resolution (Heald et al., 2015) - the best to date at these frequencies. Hurley-Walker et al. (2017) completed the GaLactic and Extragalactic All-sky Murchison Widefield Array survey (GLEAM) of the Southern hemisphere which will be described in more detail in Chapter 4.

Extragalactic sources are important because they are a significant EoR foregrounds ($\sim 25\%$ of the total power in the radio sky at low frequencies, Di Matteo et al., 2002) and they provide the models to calibrate interferometric observations (see Chapter 3). Their spatial and spectral characterization is therefore important to define accurate calibration models. Bright (> 1 Jy) radio sources typically have featureless, power-law spectra, with an average spectral index $\langle\beta\rangle = 0.78$, typical of AGN–like sources (see e.g., Cohen et al., 2004; Intema et al., 2011; Mahony et al., 2016). Callingham et al. (2017), however, found that about 5% of the extragalactic population has a spectrum that peaks around 1 GHz and has a curvature at frequencies below ~ 300 MHz, where the source flux density decreases due to synchrotron self-absorption (Rybicki & Lightman, 1986). The exact position of the spectral turn over varies, however, from source to source.

2.3 Foreground separation

Foregrounds can be separated from the 21 cm signal using their different spectral properties. Synchrotron emission is spectrally featureless (smooth) over tens of MHz (e.g., Shaver et al., 1999; Santos et al., 2005), whereas the 21 cm signal is expected to spectrally vary over MHz scales due to its redshift evolution (Santos et al., 2005). Foregrounds can therefore be modeled and removed/subtracted, or "avoided". I will describe these two approaches in the next sections.

2.3.1 Foreground removal

Foreground subtraction is generally envisioned to happen in two stages, where bright, compact sources are subtracted first and diffuse Galactic synchrotron emission is then removed together with the confusion-like contribution from extragalactic sources (e.g. Morales et al., 2006).

Bright compact sources are modelled and then subtracted from the interferometric visibilities in order to achieve the greatest accuracy possible (e.g., Noordam & de Bruyn, 1982; Bernardi et al., 2010). This step often involves an extra calibration step that corrects specific instrumental or ionospheric distortions (e.g., Mitchell et al., 2008; Bernardi et al., 2010; Yatawatta et al., 2013).

After subtraction of bright compact sources, diffuse emission remains much brighter than the 21 cm signal (Morales et al., 2006). Subtraction of diffuse emission can be carried out in a parametric or non-parametric fashion. Parameteric methods assume that foregrounds can be modeled by functional forms whose parameter are fitted to the data. For instance, Bowman et al. (2009) subtracts foregrounds from simulated sky maps by fitting a third-order polynomial along the spectral dimension of each pixel (i.e each line of sight) in the data cubes.

Non-parametric methods avoid to assume any specific form for the foregrounds and instead use the data properties to define the foreground model. For example, the "Wp" smoothing technique (Harker et al., 2009, 2010) fits a function along each line of sight of an image cube where changes of the spectrum curvature - which should not appear in synchrotron emission - are penalized. Chapman et al. (2013, 2016) introduce a foreground modeling and subtraction method based on the Generalized Morphological Component Analysis (GMCA, Bobin et al., 2007), which uses morphological differences to separate different components. In the EoR application, it assumes the existence of a basis set where the spectrally-smooth foregrounds components are sparse, i.e. are represented by few coefficients, and can, therefore, be separated from the residual EoR signal and the noise.

2.3.2 Foreground avoidance

Alternatively to modeling and subtraction, foregrounds can be 'avoided": the frequency dependent response of an interferometric array imposes a specific pattern to the frequency-smooth foregrounds that can be more easily seen in power spectrum space. The spherically averaged power spectrum $P(k)$ (equation 1.4) can be separated along a component parallel and perpendicular to the line of sight $P(k_\parallel, k_\perp)$ with:

$$k_\perp = \frac{2\pi \frac{\mathbf{b}}{\lambda}}{D(z)}, \quad k_\parallel = \eta \frac{2\pi \nu_{\rm HI} H_0 E_z}{c(1+z)^2}, \tag{2.3}$$

where $\mathbf{b}$ is the baseline vector (which will be discussed in Chapter 3), λ is the observing wavelength, $D(z)$ is the transverse comoving distance at a given z, η is the Fourier conjugate of the observing frequency, $\nu_{\rm HI} = 1420$ MHz is the rest frequency of 21 cm

radiation. H_0 and $E(z) = \sqrt{\Omega_m(1+z)^3 + \Omega_k(1+z)^2 + \Omega_\Lambda}$ are standard cosmological terms. In this representation, foreground emission is expected to be bound to a wedge-like region in $(k_\parallel, k_\perp)$, and the EoR remains the brightest (in principle) signal in the remaining region (Figure 2.2; Datta et al., 2010; Pober et al., 2013; Moore et al., 2013; Kohn et al., 2016; Nunhokee et al., 2017; Kohn et al., 2018).

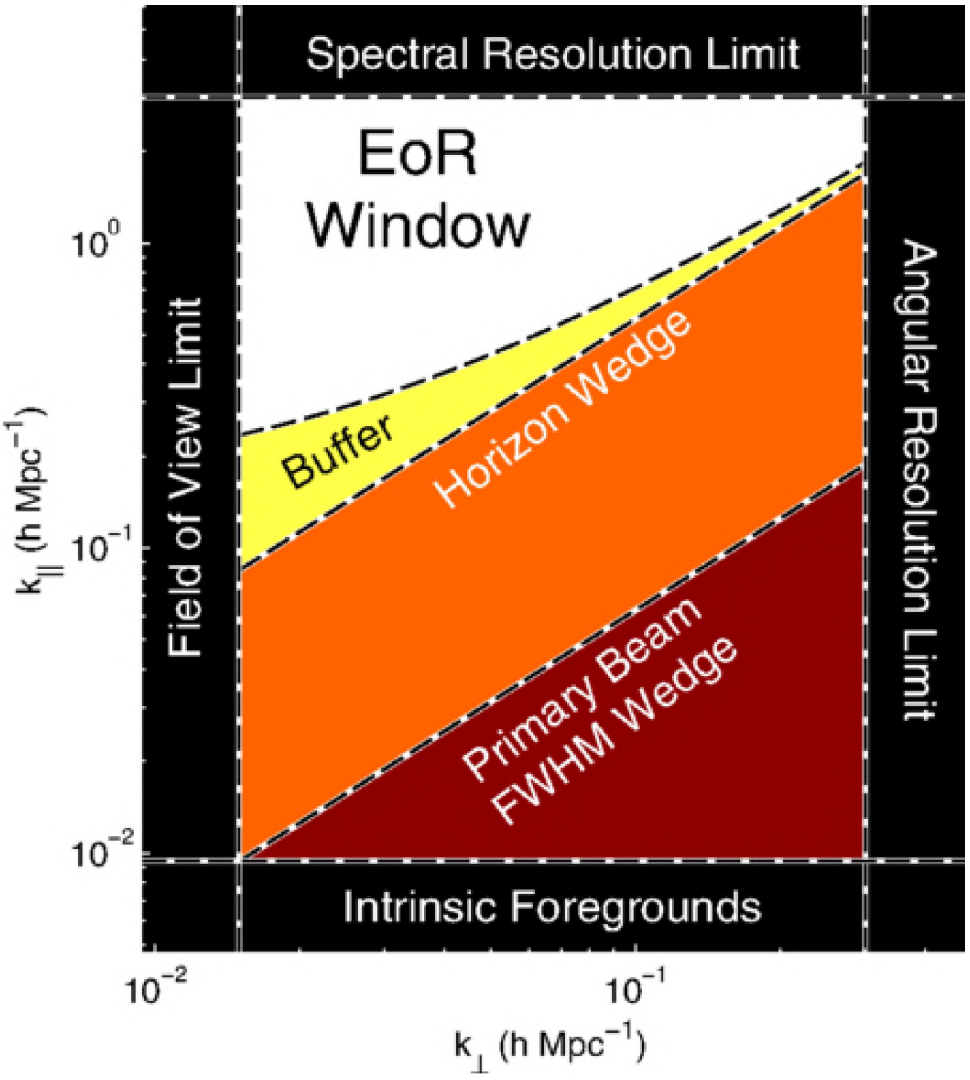

FIGURE 2.2: An illustration of foreground avoidance EoR window and the foregrounds' wedge in the foreground avoidance scheme (Dillon et al., 2015).

Pober et al. (2013) was the first to actually observe the foreground wedge with a remarkable match to the expectations (Figure 2.3). They found that, however, foreground emission extends beyond the theoretical horizon limit, in particular at low $k_\perp$ modes where the Galactic foregrounds are brighter.

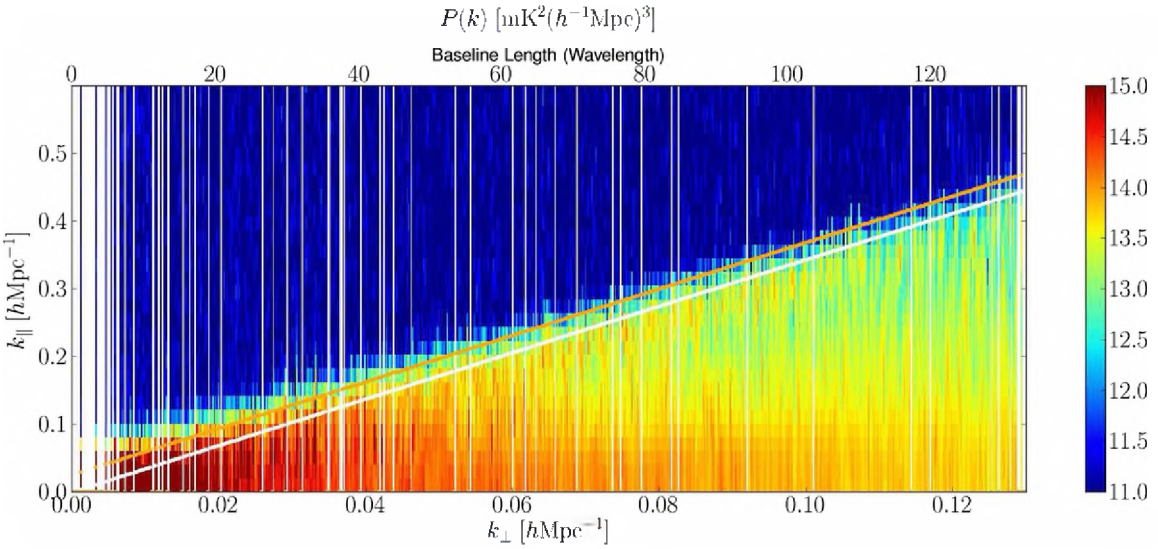

FIGURE 2.3: The foreground wedge and the EoR window from PAPER data (Pober et al., 2013).

2.4 Thesis motivation

The biggest challenge to the EoR detection is therefore to separate its signal from the foreground emission. To date, it is not clear if foregrounds can be simply avoided or some mixed approach that includes modeling/subtraction and avoidance is needed. Current EoR limits seem to show foreground contamination in the EoR window likely due to systematic errors (e.g., Beardsley et al., 2016; Patil et al., 2016; Cheng et al., 2018). Foreground modeling and subtraction may reduce the contamination into the EoR window (Pober, 2015; Kerrigan et al., 2018). In particular, observations carried out with wide field of view telescopes may need the subtraction of an all-sky foreground model in order to obtained a "cleaner" EoR window (Pober et al., 2016). Such foreground model is composed, in the first place, of bright extragalactic sources that are, also, the model used for interferometric calibration (see Chapter 3): these are the motivation of this thesis work. In this thesis I present the analysis of 300 hours of PAPER observations taken with 128 dipoles (see Chapter 3). I focus on obtaining large-area images that are then used to extract a source catalogue. The obtained large-area sky catalogue is used to confirm the accuracy of the calibration procedure and to provide a high accuracy foreground model to be used for foreground mitigation and calibration of EoR observations.

Chapter 3

Calibration and imaging of PAPER observations

3.1 Basics of radio interferometry

Radio interferometry is a technique in which many radio antennas are combined to simulate a single element (synthesised telescope). An array that uses this technique is known as an interferometer. The angular resolution θ of an interferometer is given by:

$$\theta \sim \frac{\lambda}{B_{\max}}, \tag{3.1}$$

where λ is the observing wavelength and $B_{\max}$ is the maximum baseline, i.e. the maximum separation between a pair of antennas. The simplest form of an interferometer is the two-element interferometer (Figure 3.1): it measures the coherence of the signal received by a pair of antennas from a source of electromagnetic radiation.

The signal from a celestial source along the direction $\hat{\mathbf{s}}$ reaches antenna j later than antenna i, with a delay, τ_g, that depends upon the the baseline $\mathbf{b}$ (Thompson et al., 2017):

$$\tau_g = \frac{\mathbf{b} \cdot \hat{\mathbf{s}}}{c}, \tag{3.2}$$

where c is the speed of light and a cartesian coordinate system (u, v, w) is used to describe the baseline, with w pointing to the direction of the source. It can be demonstrated (e.g., Thompson et al., 2017) that the visibility V is related to the sky brightness distribution I as:

$$V(u,v,w) = \int\int A(l,m) I(l,m) e^{-2\pi i(ul+vm+w(\sqrt{1-l^2-m^2}-1))} \frac{dl\, dm}{\sqrt{1-l^2-m^2}}, \tag{3.3}$$

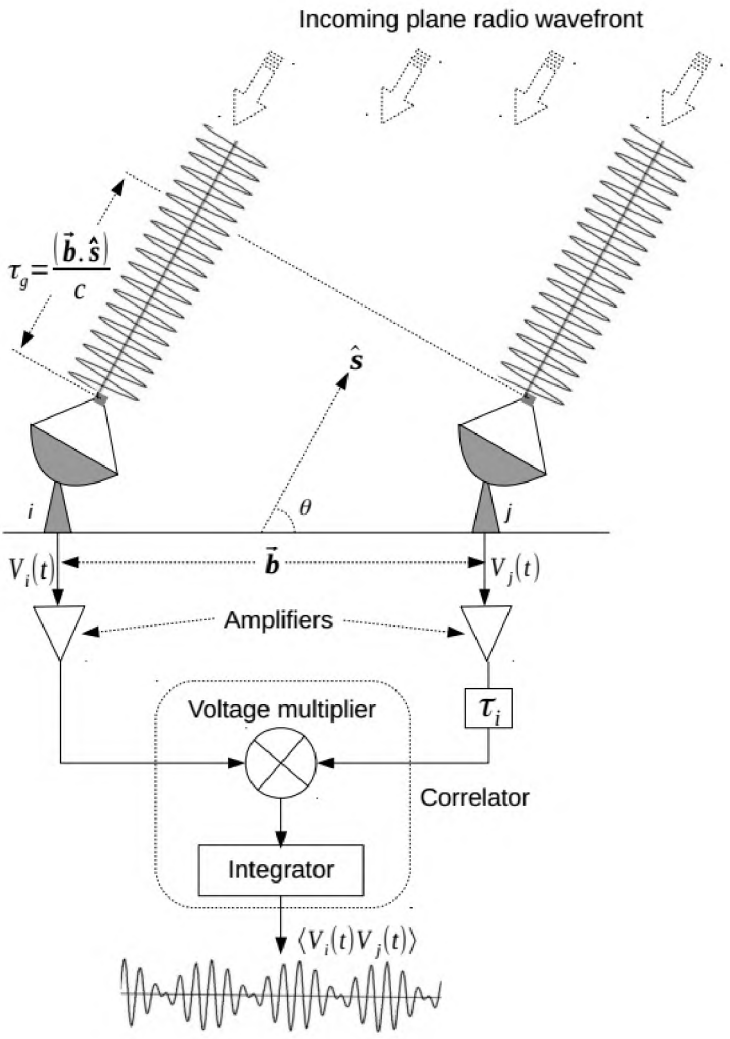

FIGURE 3.1: A schematic representation of the two element interferometer. The signal reaches antenna j before antenna i thus a delay is introduced in the signal from j before both signals are correlated to get the visibilities (Liju, 2016).

where A represents the instrumental response as a function of the effective collecting area and the direction of the incoming signal, and (l, m) are the directions cosines.

If we assume that the observation is made with a coplanar array (i.e. $w = 0$) or over a small field of view ($\sqrt{1 - l^2 - m^2} \approx 1$), equation 3.3 becomes:

$$V(u, v) = \int \int \tilde{I}(l, m)\, e^{-2\pi i(ul+vm)} dl\, dm, \tag{3.4}$$

where $\tilde{I}(l, m) = A(l, m)\, I(l, m)$. Equation 3.4 is a two dimensional Fourier transform and is often referred to as the Van Cittert-Zernike theorem.

The sky brightness can therefore be obtained, in principle, through an inverse Fourier transform:

$$\tilde{I}(l,m) = \int\int V(u,v)\, e^{2\pi i(ul+vm)} du\, dv. \tag{3.5}$$

3.2 Calibration

In practice, the celestial radio signal encounters several corruptions due to atmospheric/ionospheric opacity and instrumental effects before being recorded. Calibration is the process that aims to correct such corruptions and is usually described via the Radio Interferometry Measurement Equation (RIME, e.g., Smirnov, 2011a) formalism. In the RIME, instrumental corruptions are represented by 2×2 matrices $\mathbf{J}$ (Smirnov, 2011a):

$$\mathbf{V}_{pq} = \mathbf{J}_p \left(\int_l \int_m \mathbf{B}_{pq}\, e^{-2\pi i(u_{pq}l + v_{pq}m)} dl dm \right) \mathbf{J}_q^H, \tag{3.6}$$

where $\mathbf{V}_{pq}$ is a 2×2 visibility matrix that includes the x and y polarisation products,

$$\mathbf{V}_{pq} = \begin{pmatrix} V_{pq}^{xx} & V_{pq}^{xy} \\ V_{pq}^{yx} & V_{pq}^{yy} \end{pmatrix}, \tag{3.7}$$

for antenna p and q, ^{H} denotes the Hermitian conjugate and $\mathbf{B}$ is a model of the sky brightness distribution in the (l,m) plane:

$$\mathbf{B} = \begin{pmatrix} I+Q & U+iV \\ U-iV & I-Q \end{pmatrix}. \tag{3.8}$$

I, Q, U and V in equation 3.8 are the Stokes parameters which describe the state of polarisation for an electromagnetic wave.

In calibration, $\mathbf{B}$ is defined by the calibration source(s). A calibration source is generally a point source whose flux density spectrum and position are known and it is not variable over the observation time-scale. A calibrator source should also be sufficiently bright and isolated from nearby confusing sources in order to achieve a high signal to noise ratio measurement. Using such a calibrator source, the Jones matrices can be determined via a non-linear fit of the model to the visibility data. Once the Jones matrices are calculated, corrected visibilities $\widehat{V}$ can be formed as:

$$\widehat{V}_{pq} = \mathbf{J}_p^{-1} V_{pq} \mathbf{J}_q^{H^{-1}}. \tag{3.9}$$

This process is referred to as the first generation calibration (1GC).

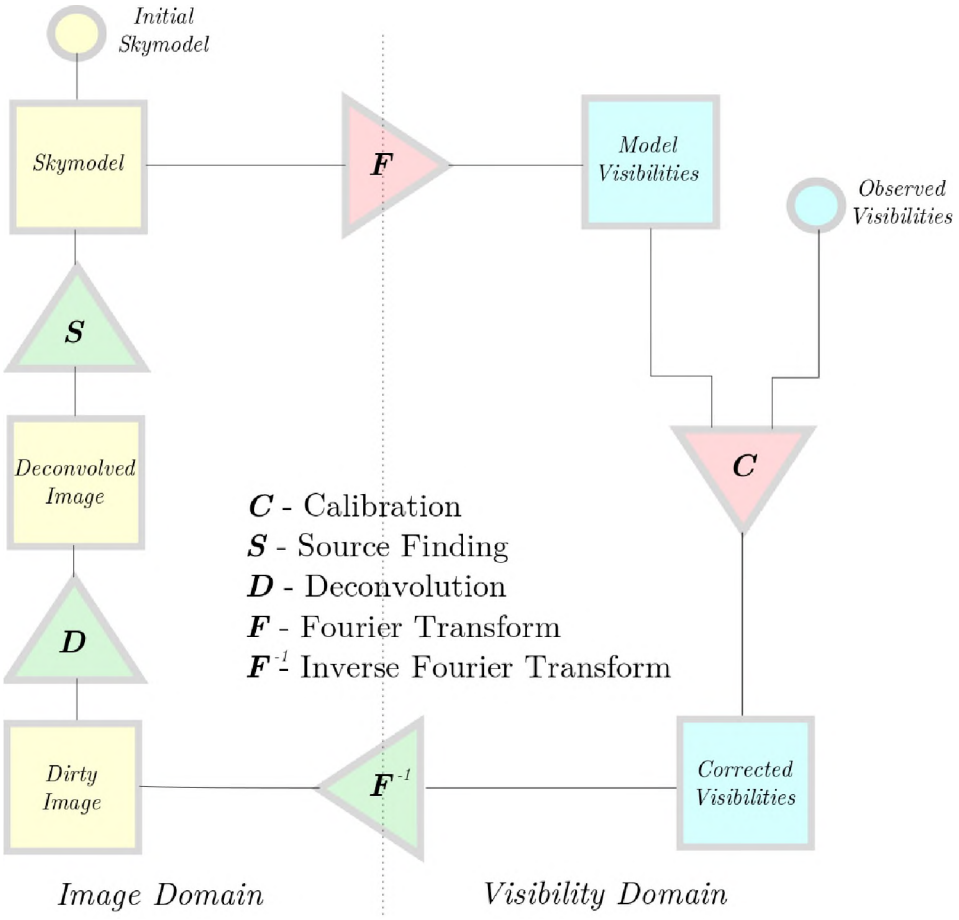

FIGURE 3.2: A schematic representation of the general self-calibration procedure. The image domain and the visibility domain are linked by the Fourier and the inverse Fourier transforms.

After 1GC, self calibration is usually applied as the second generation calibration (2GC) (Taylor et al., 1999). It makes use of the observed field itself to further calibrate the visibilities. Generally, 2GC is done iteratively, switching between two domains: the image domain and the visibility domain until the desired results are obtained or there is no more improvement achieved in the image. In the image domain deconvolution and source finding are performed, while calibration takes place in the visibility domain. Self calibration generally involves the following steps (Figure 3.2):

1. Obtaining an initial sky model: This can be obtained from deconvolution or from an external source catalogue;
2. deriving gain solutions by using the model. Correcting the visibilities;
3. deconvolving the image to obtain an updated model;
4. repeating steps 2 and 3 until satisfactory results are obtained.

For completeness, we mention the relatively recent third generation calibration (e.g., Smirnov, 2011b) that corrects for direction dependent corruptions. This form of calibration is, however, not applied in this work.

3.3 The Precision Array to Probe the Epoch of Reionization

PAPER is a 128 element array located at the Square Kilometer Array South Africa reserve, in the Karoo desert, Northern Cape province of South Africa, about 60 km west of Carnarvon town. It is an experiment focused on measuring the power spectrum of the 21-cm line (Parsons et al., 2010). The array employs drift-scanning, dual-polarisation dipole antennas tuned for efficient operation in the 100 to 200 MHz frequency range. Since November 2011, it has been arranged in a maximally redundant grid configuration to achieve high sensitivity on a limited number of power spectrum modes (Parsons et al., 2012). Table 3.1 gives a summary of the PAPER observational set up used in this thesis. Dipoles outside the redundant configuration (outriggers) were also added to improve the *uv* coverage.

TABLE 3.1: Summary of the observational setup.

Array latitude	$-30°43'17''$
Array longitude	$21°25'40''.08$
Number of dipoles	128
Frequency range	$100 - 200$ MHz
Frequency resolution	495 kHz
Right ascension range	$0^h < \alpha < 16^h$
Declination centre	$30°43''17'$

This thesis used observations carried out with a total of 128 dipoles which comprised of 112 redundant dipoles arranged in a 16×7 rectangular grid configuration and 16 outriggers, for 29 days between February and March 2014. Figure 3.4 shows the LST coverage as function of observing day.

In the data preprocessing stage, frequency channels known to be affected by persistent RFI were flagged. Further RFI was flaggged using the delay/delay-rate filter technique (Parsons & Backer, 2009) that also served as a data compression method to reduce the data volume by over a factor of 40. The 2048 initial channels in the 100 MHz bandwidth are compressed to 203 channels with a frequency resolution of $\sim$495 kHz. The data has an integration time of 42 seconds resulting in 14 time samples for each snapshot.

FIGURE 3.3: PAPER element.

3.3.1 Data calibration

The Common Astronomy Software Applications (CASA) package was used in this work, complemented by custom developed Python scripts. Each snapshot visibility data was flagged using the *flagdata* task in CASA as follows:

1. All data below 120 MHz and also data above 180 MHz were flagged due to the sensitivity loss at the edge of the band (e.g., Kohn et al., 2016);

2. visibility amplitudes as a function of frequency were inspected for each dipole, in order to identify any malfunctioning dipoles: 21 dipoles in total were permanently flagged;

3. the *tfcrop* autoflag algorithm was applied. For each channel, the algorithm first perfomed a line fit to the visibilities amplitudes along the time axis and flagged the outliers. It then averaged the data over the 10 minutes snapshot interval, applied a polynomial fit to the frequency bandwidth, and then obtained the standard deviation, σ, of the fit. Data points that deviate more than 3σ from the mean were then flagged. The process was iterated until no data was further flagged.

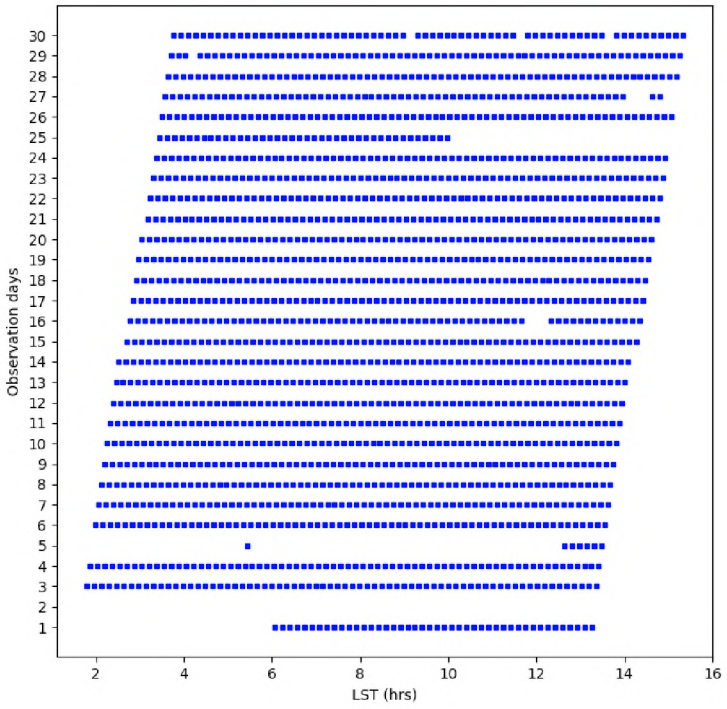

FIGURE 3.4: LST covered for all the observing nights used in this thesis. Each blue square represents a 10 minutes snapshot.

In traditional radio astronomy, first generation calibration is obtained by using sources referred to as calibrator sources (see the 1GC description given in Section 3.2). Observations of the target field are interspersed with calibrator observations that are used to determine the antenna gains. This is usually an effective method to correct for time variability of the antenna gains. Calibration sources are, however, not well isolated in PAPER observations given its $\sim 45°$ full width at half maximum primary beam at 150 MHz. Despite this potential limitation, we chose to approach the calibration problem by using a single bright source to determine the dipole complex gains. Even though a single point source is far from being an accurate description of the sky brightness sensitivity seen by the PAPER beam, this approach enables the calibration of both the dipoles arranged in the redundant configuration and the outriggers, which would not be possible by using redundant calibration techniques only (e.g., Liu et al., 2010; Zheng et al., 2014).

Pictor A was chosen as the only calibrator source in our sky model. The main motivation behind this decision is that, at the resolution of our observations ($\sim 24'$), Pictor A is the brightest unresolved source in the field of view. Additionally, it has a known, featureless

power law spectrum in the $100 - 200$ MHz range (Jacobs et al., 2013):

$$S(\nu) = S_{150} \left(\frac{\nu}{150 \text{ MHz}} \right)^{-\alpha}, \tag{3.10}$$

where $S(\nu)$ is the flux density at the frequency ν, $S_{150} = 381.88 \pm 5.36$ is the flux density at 150 MHz and $\alpha = 0.76 \pm 0.01$ is the spectral index.

Calibration was performed once every observing day as follows:

1. The snapshot where Pictor A is closest to zenith was selected as it is the one where the source has the highest signal to noise ratio;
2. we generated a sky model consisting of a point source component with a 1 Jy flat spectrum at the position of Pictor A;
3. model visibilities were generated by Fourier transforming the model point source component;
4. we solved for antenna-based complex gains as a function of frequency. This was done using the *bandpass* task in CASA. Solutions were computed over a 10 minute interval. Only baselines longer than 12 wavelengths were considered in this step as the short baselines are more sensitive to diffuse emission which was not included in our sky model. These solutions were used to calibrate the observed visibilities.

Examples of gains solutions are shown in Figure 3.5 and 3.6. Amplitudes have a behaviour that repeats similarly over days, indicating a fair stability with time. The phase behaviours are also fairly consistent across different days, and their wraps are mostly due to uncorrected cable lengths. We then computed the variations of the gains amplitude solutions from the mean. We used the amplitude solutions from each individual frequency channel, slicing across all the observing days, to evaluate the coefficient of variation, $\sigma_r(\nu)$. This is given by the ratio of the standard deviation, $\sigma(\nu)$, and the average, $\mu(\nu)$, of the amplitude solution:

$$\sigma_r(\nu) = \frac{\sigma(\nu)}{\mu(\nu)} \tag{3.11}$$

An example of $\sigma_r(\nu_i)$ for two dipoles is shown in Figure 3.7, the variation in the gains amplitude is less than 10%, for almost all of the frequency channels.

Four snapshots showed large deviations in their solutions from the behaviour seen in the other days and were discarded from the subsequent analysis together with all data for their corresponding days. These deviations in the solutions were also seen in data from the yy polarization, in all frequencies below 132 MHz, for all the observing days. The

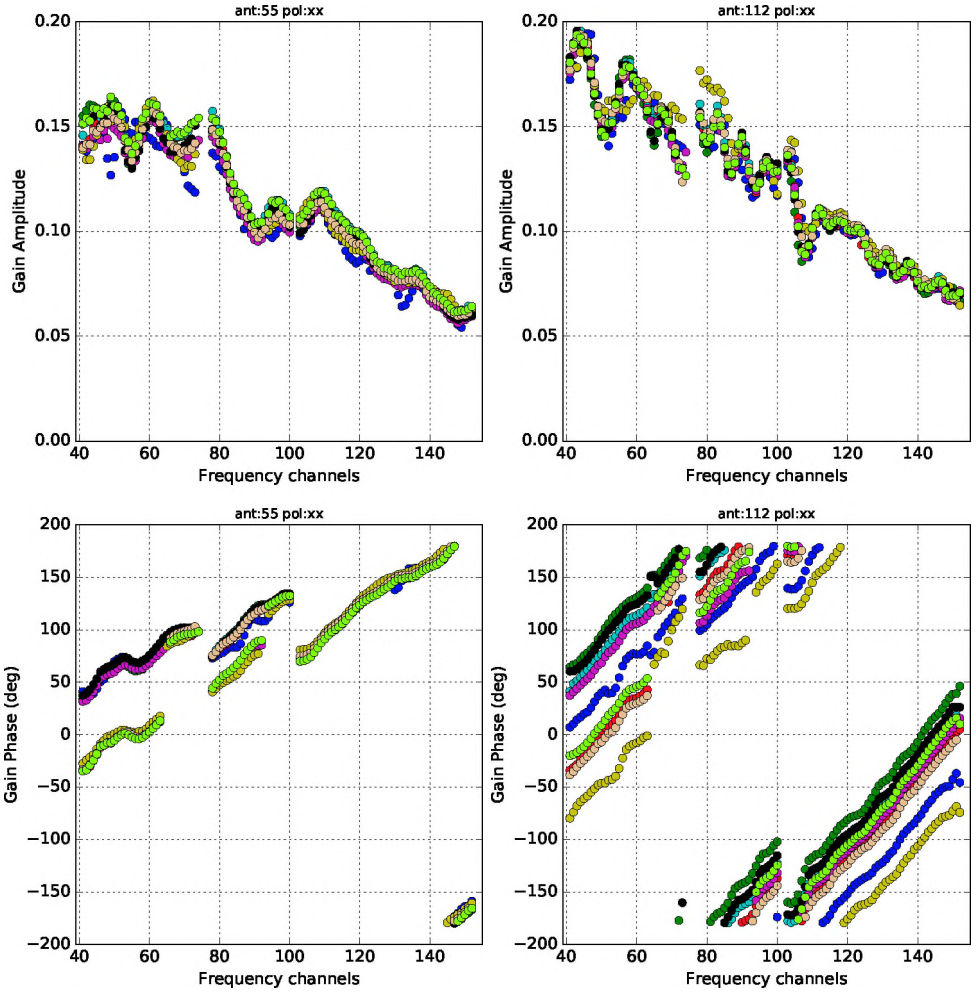

FIGURE 3.5: Gain amplitudes (top) and phases (bottom) for the xx polarisation as a function of frequency for dipoles 55 (left column) and 112 (right column) respectively for nine different nights (different colours).

corresponding data were also thus flagged. Figure 3.8 shows an example of a few days which were further flagged up to channel 75 due to bad gains.

For each snapshot observation, the calibrated visibility data were gridded into the uv-plane using the multi-frequency synthesis algorithm in CASA to improve the uv-coverage (Sault & Conway, 1999). We used uniform weights in order to achieve the maximum resolution possible. The w-projection algorithm (Cornwell et al., 2008) with 32 w-projection planes was applied to account for the array non-coplanarities. The visibilities were then Fourier transformed into $51.2° \times 51.2°$ images using the CASA task *clean*. Dirty images were then deconvolved down to a threshold of 100 mJy using the Cotton-Schwab algorithm which reduces point spread function aliasing effects and gridding errors on

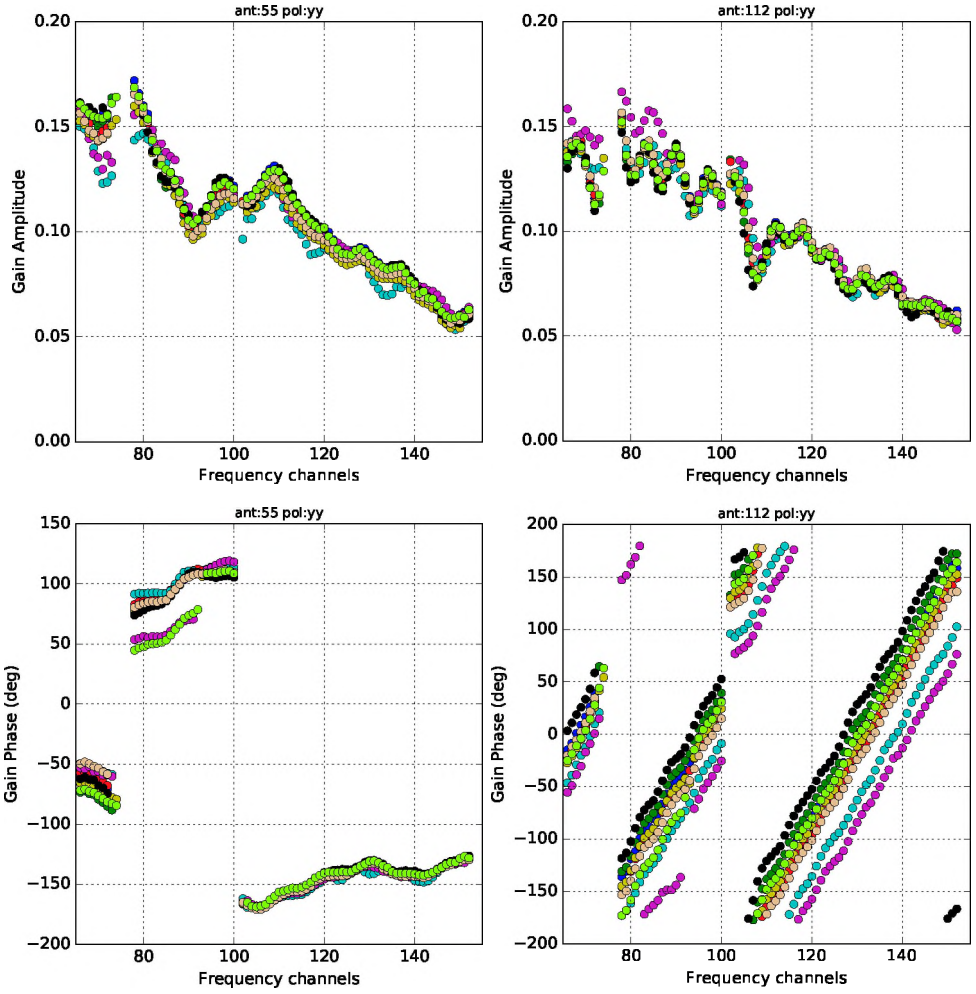

FIGURE 3.6: Same as Figure 3.5 but for the *yy* polarization.

the image (Schwab, 1984; Perley et al., 1989). An example of a deconvolved image at 150 MHz is shown in Figure 3.9. In this image we see two of the brightest sources in the field: Pictor A and Fornax A. The flux density values in the image are relative to the 1 Jy model used for calibration and the image is not corrected for the primary beam.

After deconvolution, we proceeded to perfom further flagging based on the statistics of the residuals. Model visibilities were predicted from the deconvolved sky model and then subtracted from the calibrated visibilities in order to form residual visibilities. Ideally, these should only contain thermal noise. We separately binned the real and imaginary part of the residual visibilities including only baselines longer than 30 m. The distribution of the binned residual visibilities generally followed a Gaussian-like distribution (Figure 3.10). Visibility points outside the 3σ limits of the Gaussian best

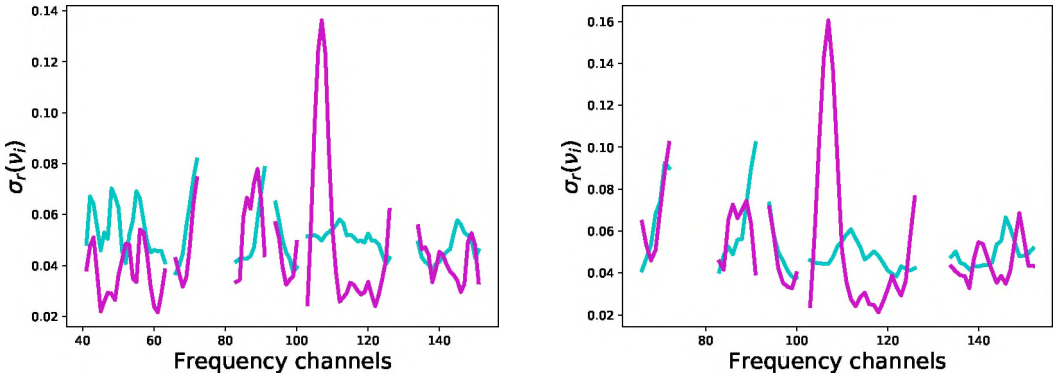

FIGURE 3.7: The coefficient of variation for the gains amplitudes per frequency channel, over the whole observing period, for antennas 55 (cyan) and 112 (magenta) for the xx (left) and yy (right) polarizations respectively.

fit were considered outliers and, therefore, flagged. Such procedure was repeated until no more data were flagged and we then re-evaluated the bandpass solutions.

3.3.2 Absolute Flux Density Calibration

The last calibration step was to bring the visibilities on a standard flux density scale. We set our flux density scale by using the Pictor A model which was also adopted by Ali et al. (2015), i.e. calculating a frequency-dependent scaling factor $F(\nu)$:

$$F(\nu) = \frac{S(\nu)\, A(\nu)}{S_m(\nu)}, \tag{3.12}$$

where $A(\nu)$ is the primary beam response evaluated in the direction of Pictor A and $S_m(\nu)$ is the measured Pictor A spectrum. Absolutely calibrated visibilities $\widehat{V}(\mathbf{b}, \nu)$ can therefore be obtained as

$$\widehat{V}(\mathbf{b}, \nu) = F(\nu)\, V(\mathbf{b}, \nu), \tag{3.13}$$

where $V(\mathbf{b}, \nu)$ represents the visibilities before the flux density scaling and $\mathbf{b}$ is the baseline vector.

To test our calibration, we derived the Pictor A spectrum for all the observation days. The snapshots used in this step are the ones in which Pictor A is closest to zenith like it was done for calibration. We first rotated the visibilities towards the position of Pictor A. We then created an image for each frequency channel and then deconvolved it down to 20 Jy. From each image, a $2° \times 2°$ postage stamp centered at the position of Pictor A was made and the source peak extracted. We oversampled the synthesized beam by using five pixels across it, in order to minimize the difference between our procedure and a full Gaussian fit to the source profile. We then proceeded to estimate

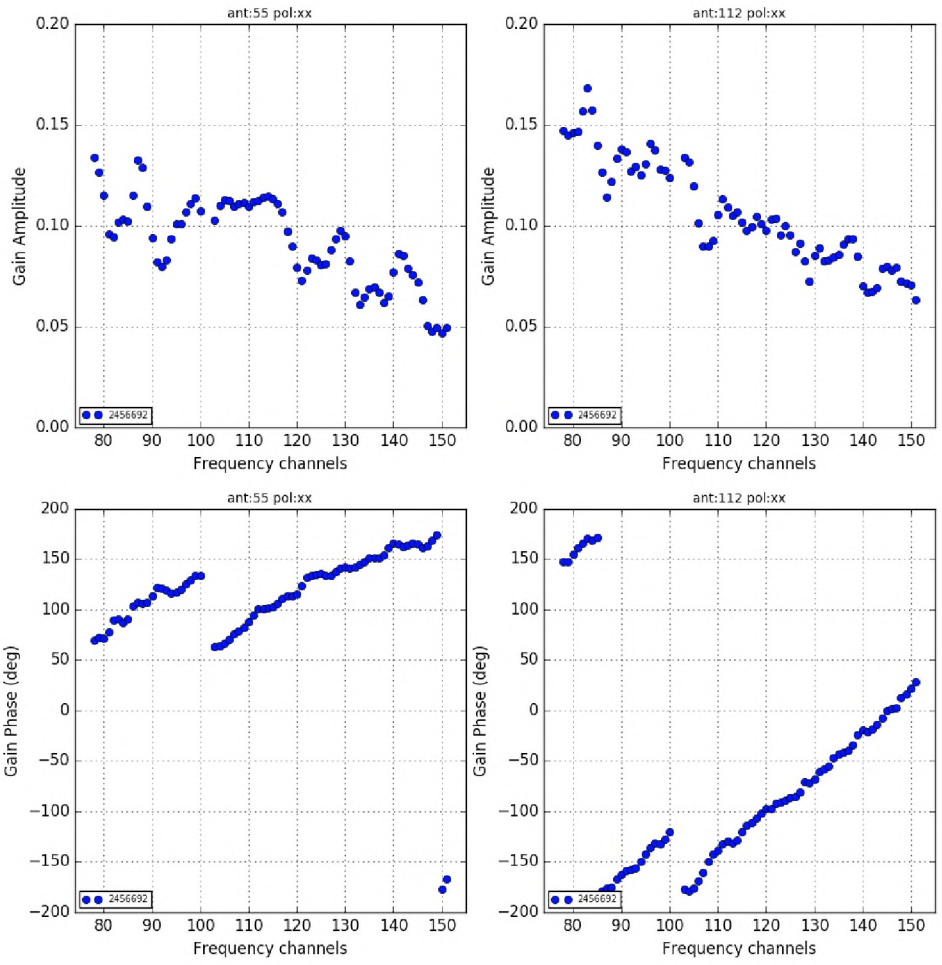

FIGURE 3.8: Gain amplitude and phase for JD 2456692 with data below channel 75 flagged.

uncertainties on the measured spectra that could account for calibration errors too. We imaged residual visibilities created by subtracting the visibilities for the Pictor A model to the calibrated visibilities in the same way described above. The uncertainty on the flux source density was estimated as the rms of the residual image.

The average spectrum $S_a(\nu)$ including all the observing days was calculated as:

$$S_a(\nu) = \frac{\sum_i S_{i,A}(\nu)\, w_i(\nu)}{\sum_i w_i(\nu)^2}, \tag{3.14}$$

where $S_{i,A}(\nu)$ is the flux per frequency channel which has first been divided by the antenna response and $w_i(\nu)$ are the weights obtained from the rms values estimated from the residual postage stamp images.

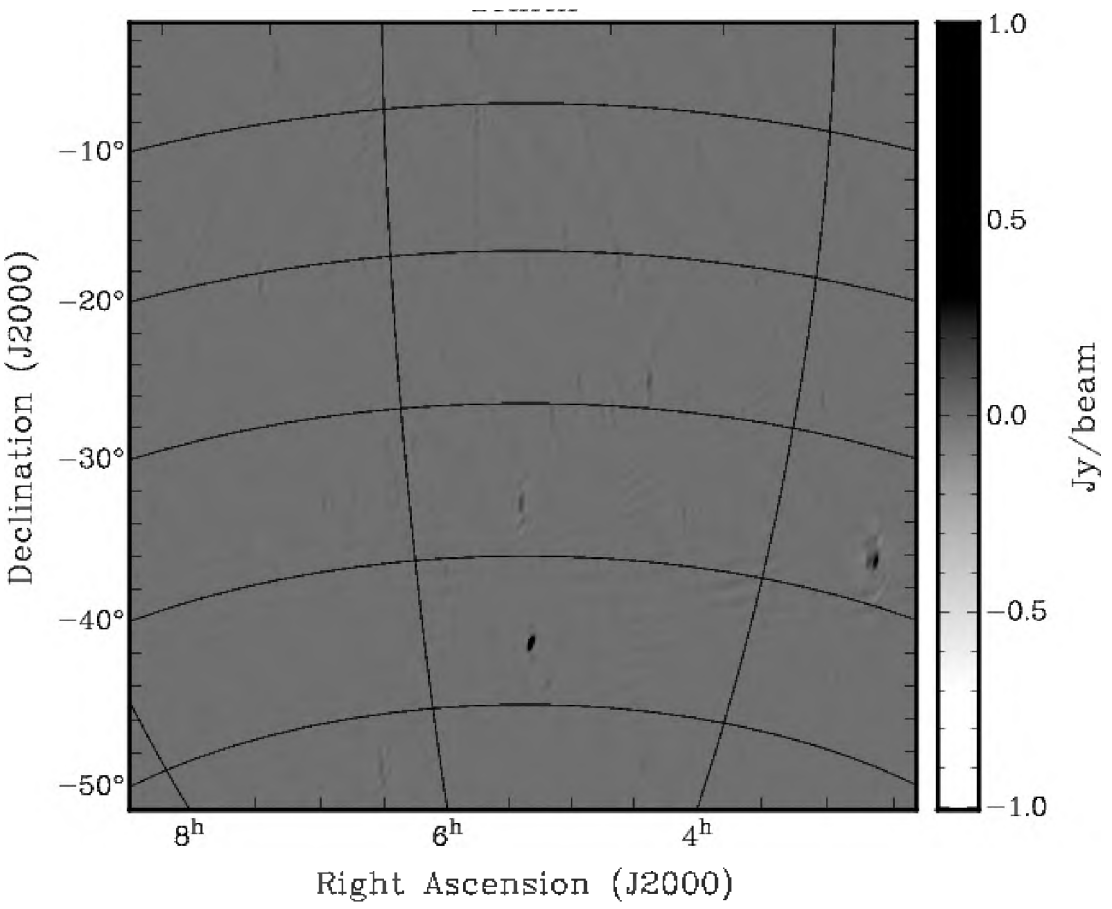

FIGURE 3.9: An image example obtained from a 10 minute snapshot calibrated data.

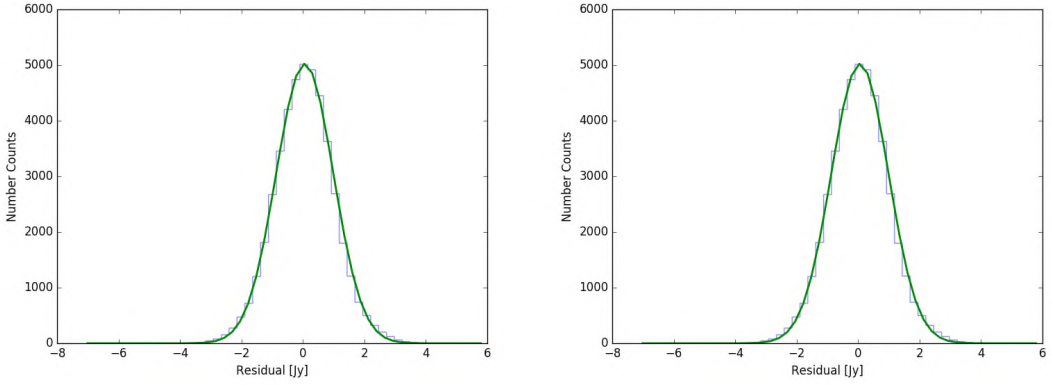

FIGURE 3.10: Gaussian fit to the real part of the residual visibilities at 156 (left) and 165 MHz (right) respectively.

A final correction in the form of a polynomial fit was applied to the average spectrum. A fifth order polynomial was fitted to the ratio between the average spectrum and the model spectrum $r(\nu)$:

$$r(\nu) = \frac{S(\nu)A(\nu)}{S_a(\nu)}, \tag{3.15}$$

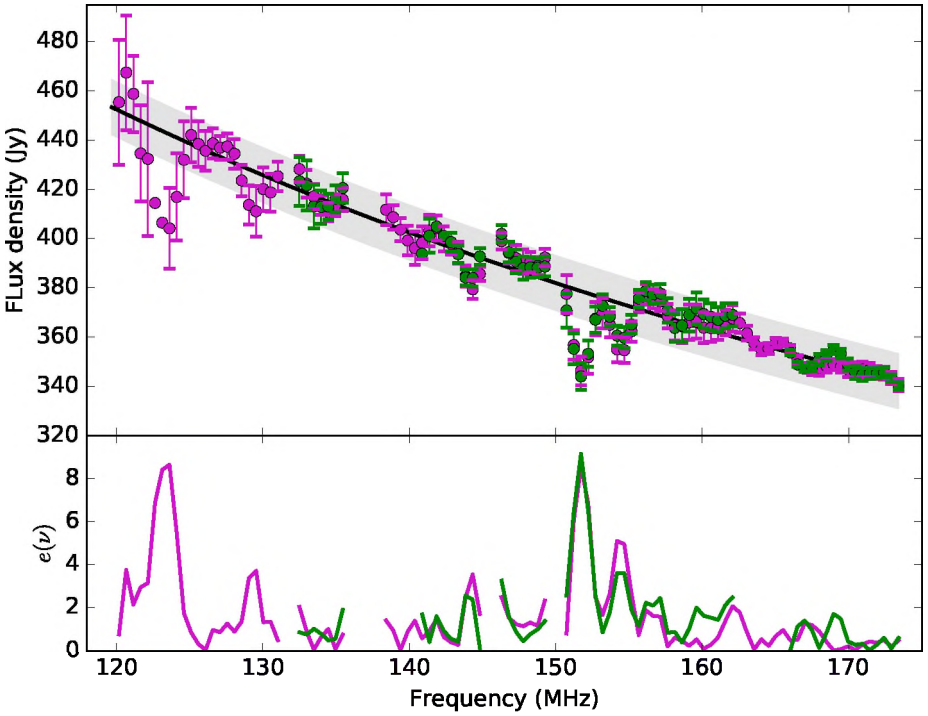

FIGURE 3.11: Pictor A average spectrum obtained for the xx (magenta) and yy (green) polarizations. The black line is the model spectrum (Jacobs et al., 2013). The lower panel shows the percentage error on the average spectrum for both xx (green) and yy (magenta) polarizations.

as:

$$\widehat{r}(\nu) = \sum_{i=0}^{n=5} r_i \, \nu^i, \tag{3.16}$$

where $\widehat{r}(\nu)$ and r_i are the fitted ratio and the coefficients of the polynomial fit respectively. The resulting best fit was used to scale the visibilities, obtaining the absolutely calibrated visibilities as:

$$\widehat{V}'(\mathbf{b}, \nu) = \widehat{r}(\nu) \, \widehat{V}(\mathbf{b}, \nu). \tag{3.17}$$

We then measured the average spectrum in the same manner described above but using now the absolutely calibrated visibilities $\widehat{V}'(\mathbf{b}, \nu)$. The final spectrum obtained is shown in Figure 3.11. The bottom panel of the figure shows the percentage error:

$$e(\nu) = \frac{|S(\nu) - \widehat{r}(\nu) S_a(\nu)|}{S(\nu)} \times 100. \tag{3.18}$$

The aim of this correction was to minimise the discrepancy between the measured spectrum and the model spectrum. The root mean square difference between the model and

the average spectra was evaluated to be 9.3 Jy. This rms value is slightly higher than the 5.4 Jy rms calculated from the model uncertainties (Jacobs et al., 2013), which might be caused by potentially bad unflagged data, remaining in our visibilities.

3.4 Sky Maps

The image formation process of long observations with non-tracking arrays faces the problem of combining visibilities whose primary beam response changes significantly with time, implying that the van Cittert-Zernike theorem is valid only instantaneously. Long integrations can either be synthesised by stacking individual snapshot images (e.g., Morales & Matejek, 2009; Ord et al., 2010; Sullivan et al., 2012; Dillon et al., 2014) or by combining visibilities in the uv plane using an appropriate time variable convolving kernel (e.g., Tasse et al., 2013). In this thesis, we followed a hybrid approach. After calibration, we first formed total intensity visibilities V_I by averaging the two orthogonal polarizations:

$$V_I = \frac{V_{xx} + V_{yy}}{2}. \tag{3.19}$$

We then grouped our snapshot observations in 2.4 hours-wide LST bins and phase rotated the visibilities of each snapshot to the centre of the LST bin. The total intensity visibilities were then imaged for each snapshot observation using the multi-frequency synthesis algorithm implemented in the CASA *clean* task. Each snapshot was deconvolved until the first negative component was found. The deconvolved snapshots had dimensions of $36° \times 36°$ with a pixel size of $3' \times 3'$ chosen for adequate sampling of the $24'$-wide synthesised beam. Uniform weighting was applied as we wanted to emphasise the compact sources which will be analysed in the next chapter. Only baselines longer than 12λ were included in the images in order to avoid large scale Galactic diffuse emission. After this process, we obtained a restored image for all the snapshots from all the days. These re-phased, deconvolved snapshot images, $I_i(t)$, were then combined together in a single image I_a, weighting them by their primary beam (e.g., Nunhokee, 2018):

$$I_a = \frac{\sum_t I_i(t) A(t)}{\sum_t A^2(t)} \tag{3.20}$$

where $A(t)$ is the primary beam correction for each snapshot and, therefore, time variable. We used the PAPER primary beam model described in Nunhokee et al. (2017), that we refer the reader to for a detailed description.

We obtained our final images spanning the $1.8\text{h} < \alpha < 17.4\text{h}$ right ascension range (Figures 3.12, 3.13, 3.14, 3.15, 3.16 and 3.17). The brightest sources in the images include Pictor A, Fornax A, Puppis A, the Crab Nebula and Centaurus A. There are

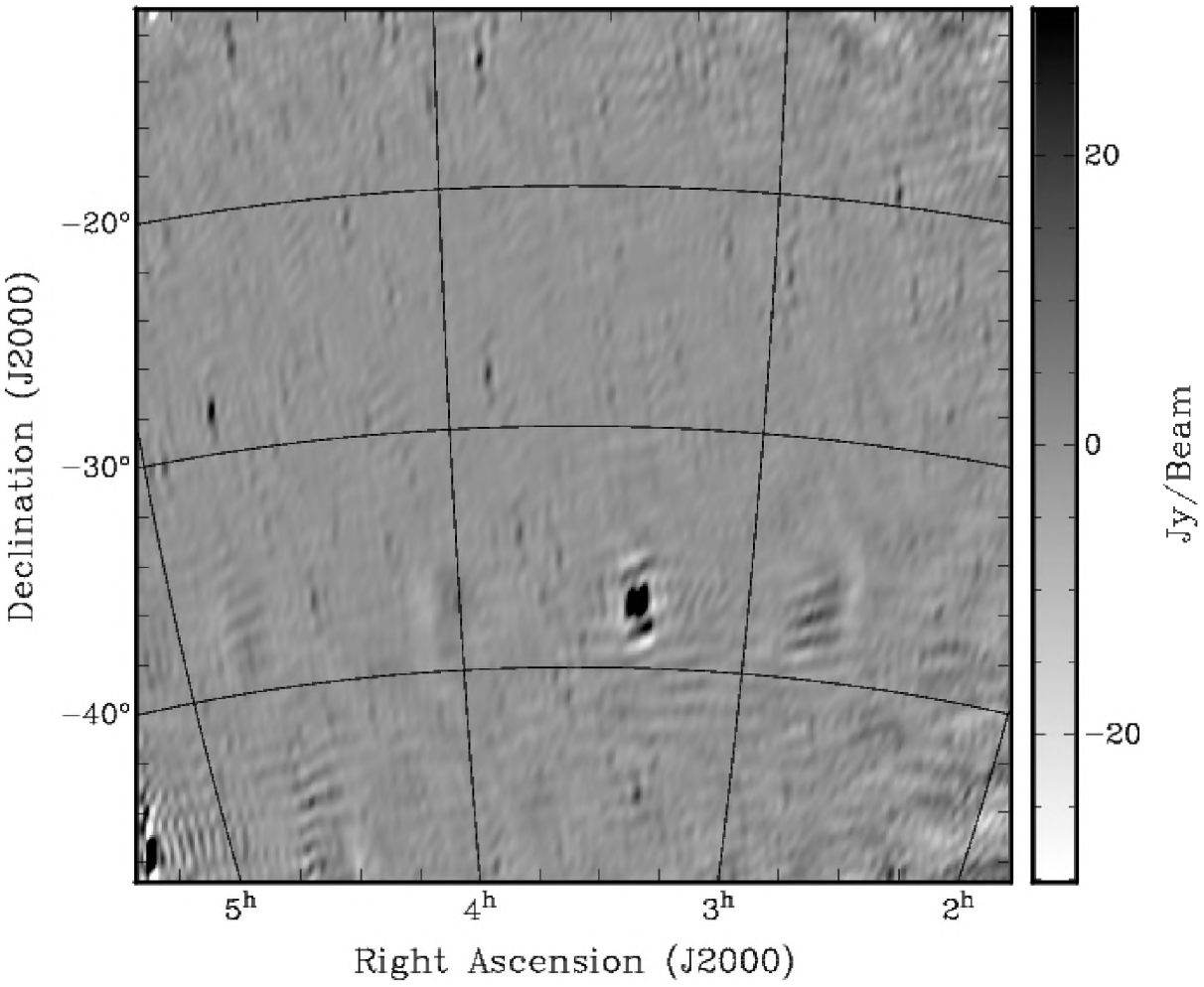

FIGURE 3.12: Total intensity map obtained from the 28 days of observations centred at LST = 3.6 hours.

residual sidelobes from these sources across the image that would require a direction dependent calibration - which we leave for future work.

We estimated the noise level in each image by calculating the image rms in small regions selected at the field edges where no bright source was present. The average of these rms values was found to be ~ 1.04 Jy beam^{-1} and it can, therefore, be considered to be the survey noise floor.

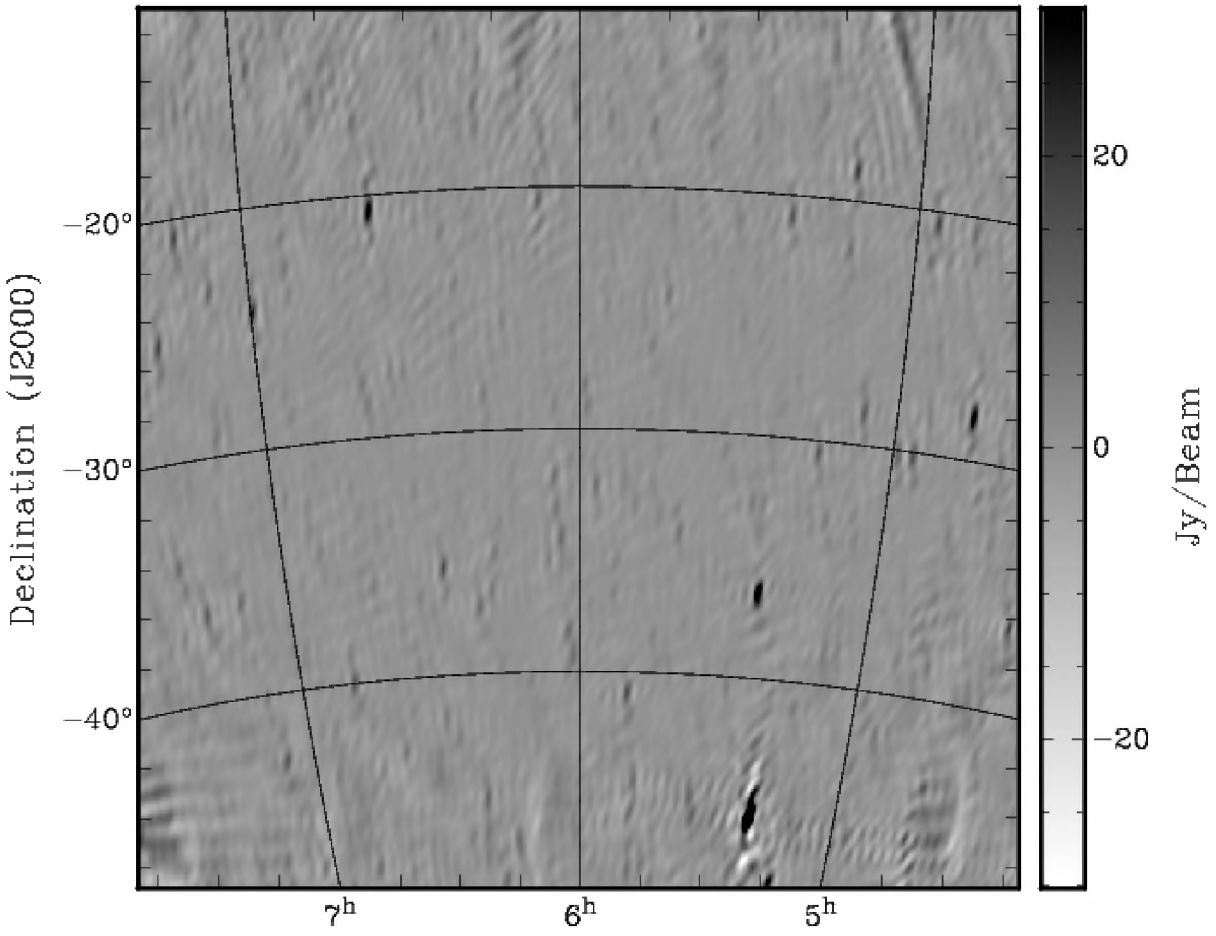

FIGURE 3.13: Same as Figure 3.12 but for the LST = 6.0 hour bin.

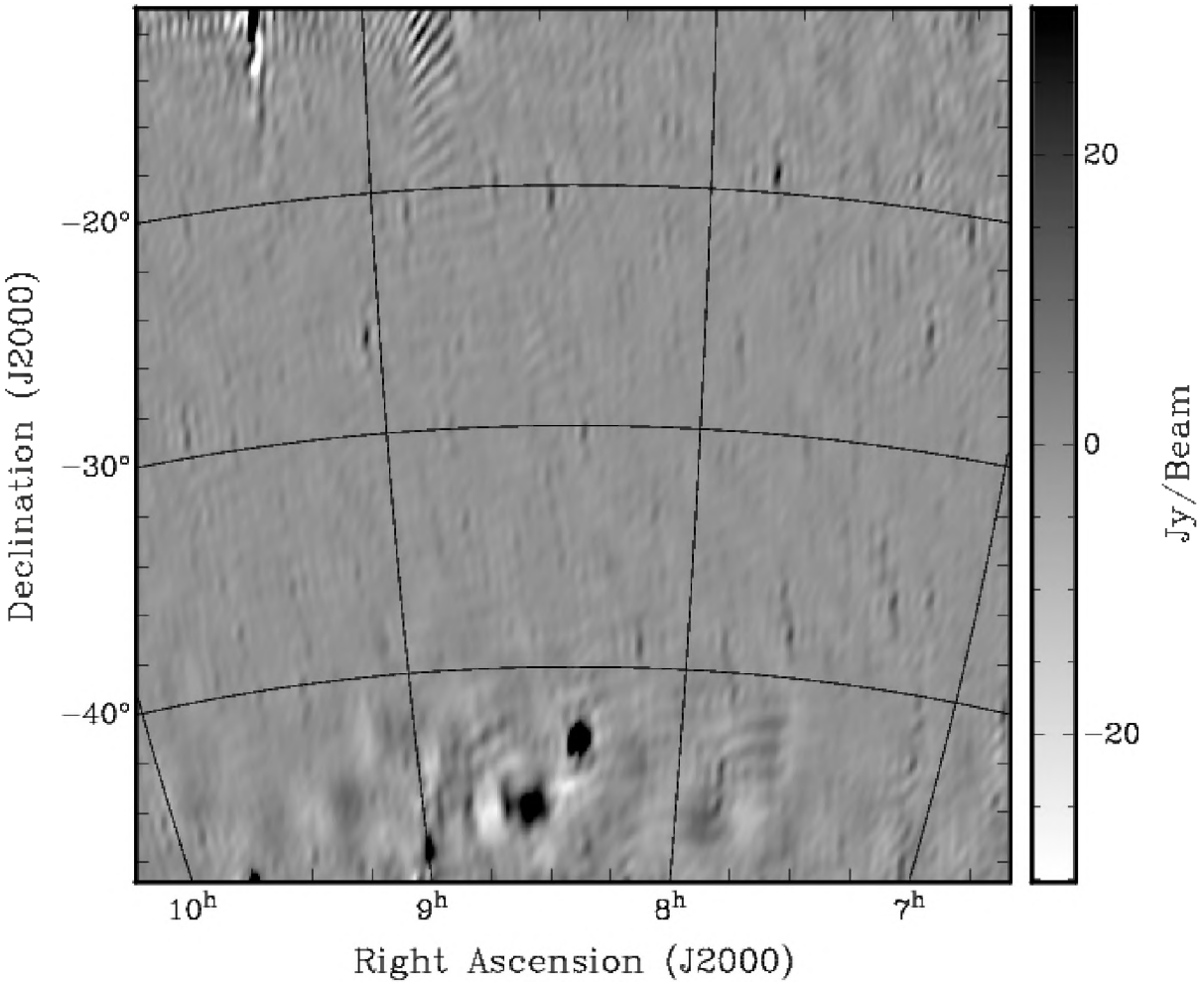

FIGURE 3.14: Same as Figure 3.12 but for the LST = 8.4 hour bin.

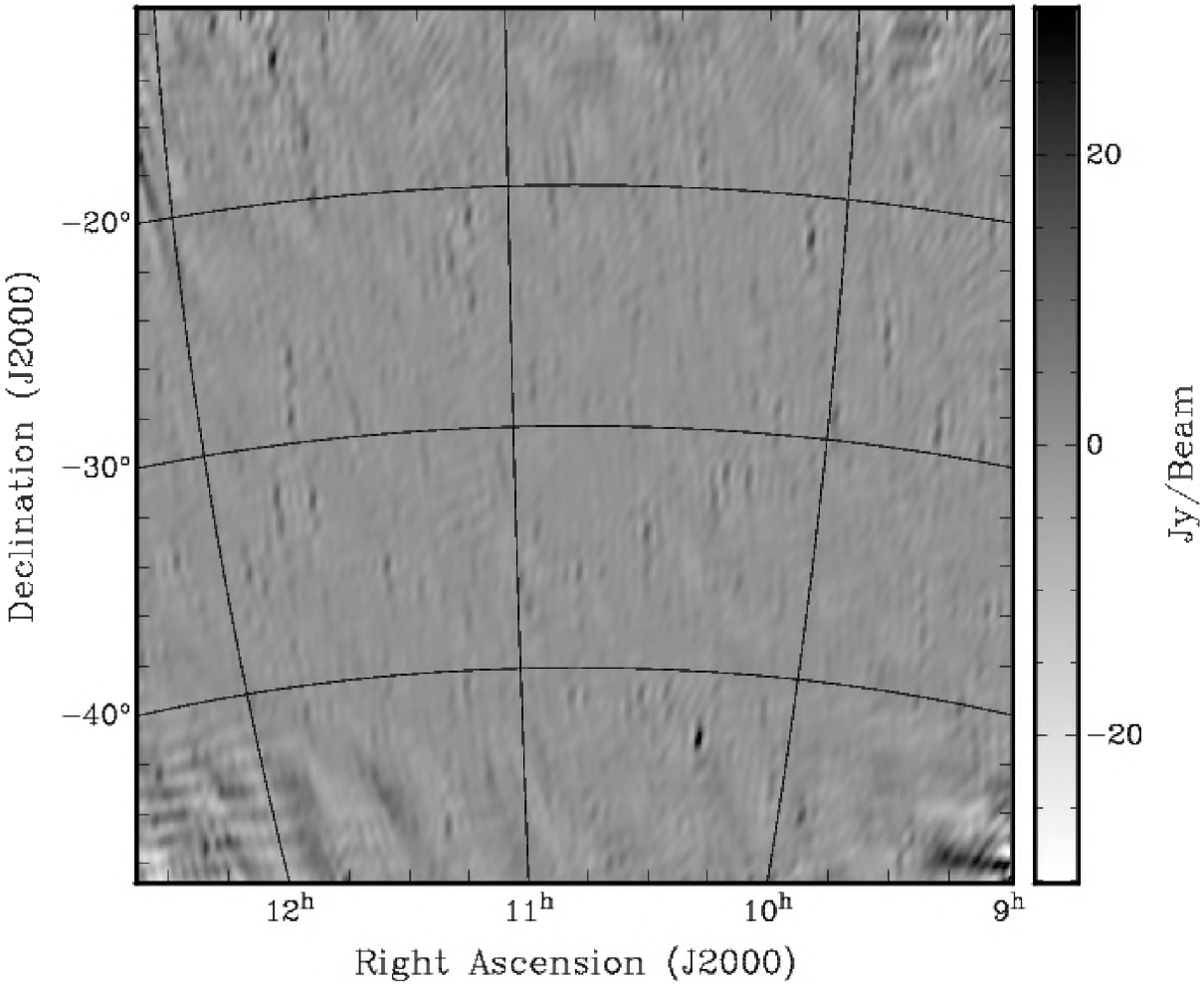

FIGURE 3.15: Same as Figure 3.12 but for the LST = 10.8 hour bin.

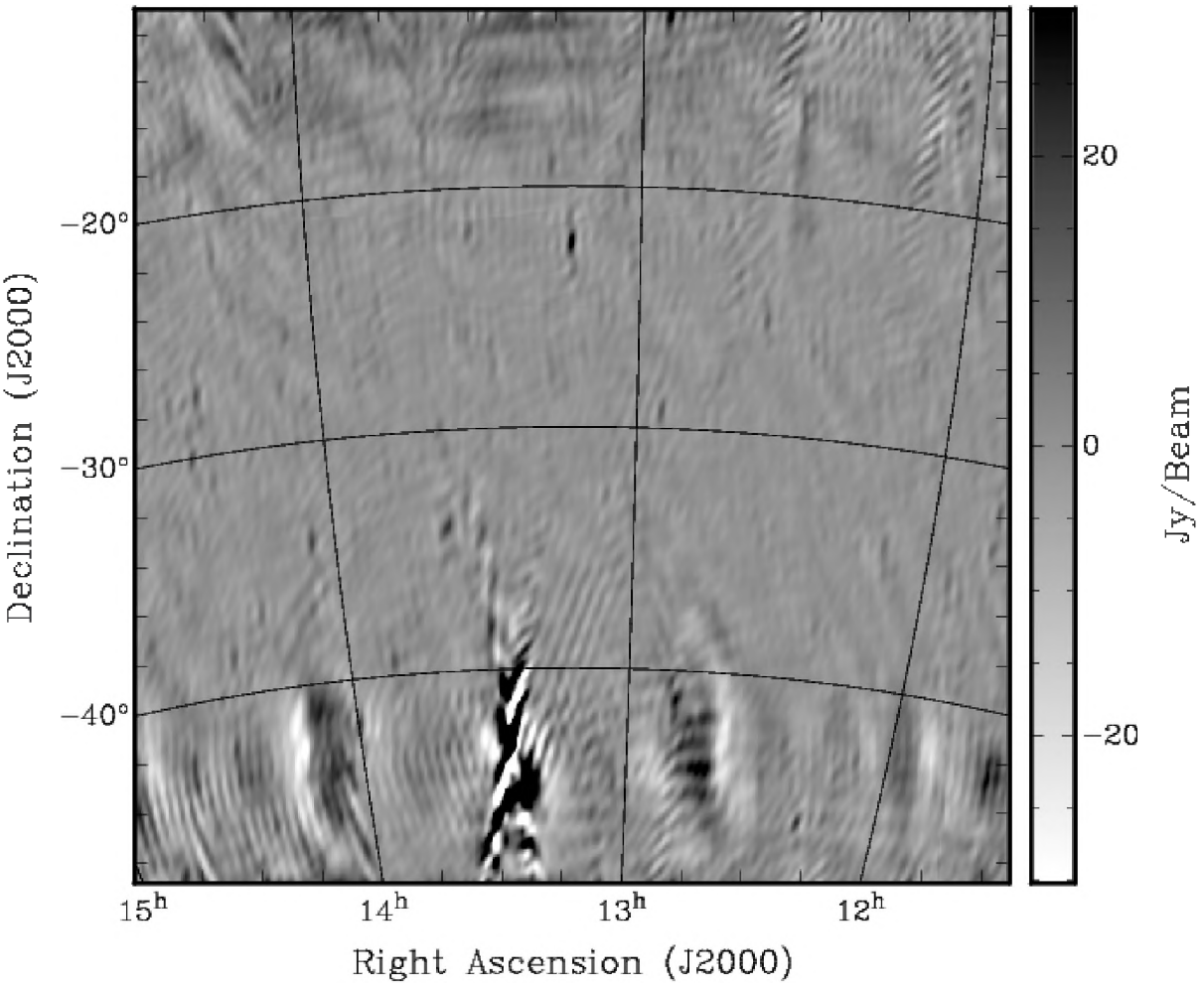

FIGURE 3.16: Same as Figure 3.12 but for the LST = 13.2 hour bin.

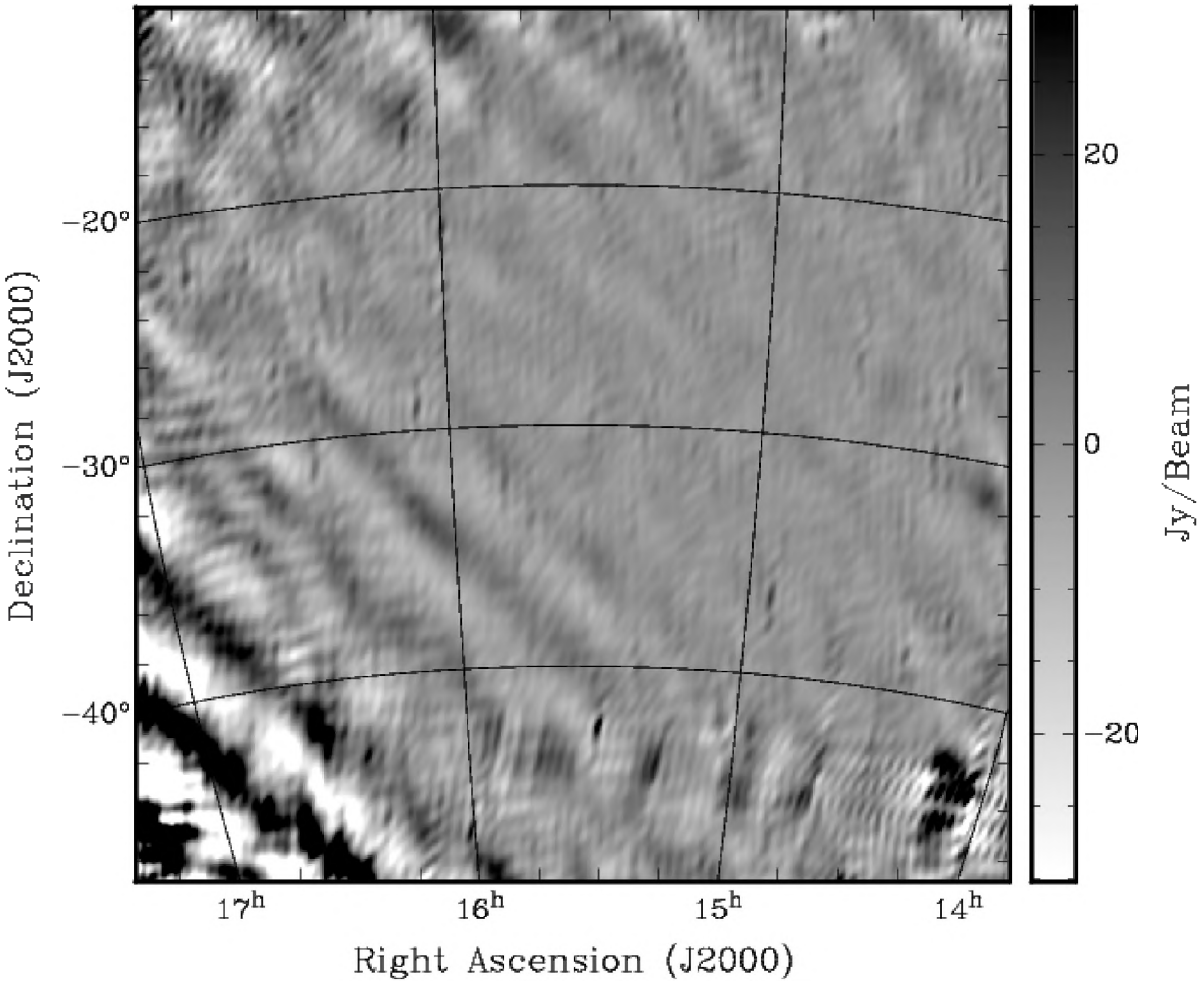

FIGURE 3.17: Same as Figure 3.12 but for the LST = 15.6 hour bin.

Chapter 4

Source Extraction and Source Catalogue

In Chapter 3, we described the data calibration and image formation procedure. In this chapter, we describe how we extracted a source catalogue from the images and compared it with literature results.

4.1 Source extraction

Source extraction requires a characterization of the image noise properties. Generally, the pixel amplitude x of radio images fairly follows a Gaussian distribution G:

$$G\left(x|\mu,\sigma\right) = \frac{1}{\sigma\sqrt{2\pi}} e^{\frac{-(x-\mu)^2}{2\sigma^2}} \tag{4.1}$$

where μ and σ are the mean and the standard deviation of the image data respectively. The mean value of an interferometric image is essentially zero by construction. If the image is noise limited, the standard deviation is a fair estimate of the noise standard deviation - whose distribution is, again, assumed to be Gaussian (Hopkins et al., 2002; Huynh et al., 2012). The observed pixel distribution is often skewed towards positive values, due to the presence of sky sources.

Our images are in several ways different than the case described above as they are not fully deconvolved and do not take advantage from a full uv rotation synthesis. We found, however, that the distribution of the pixel values is fairly Gaussian in our case too, with high tails however (Figure 4.1 shows an example for the LST = 10.8 hours image).

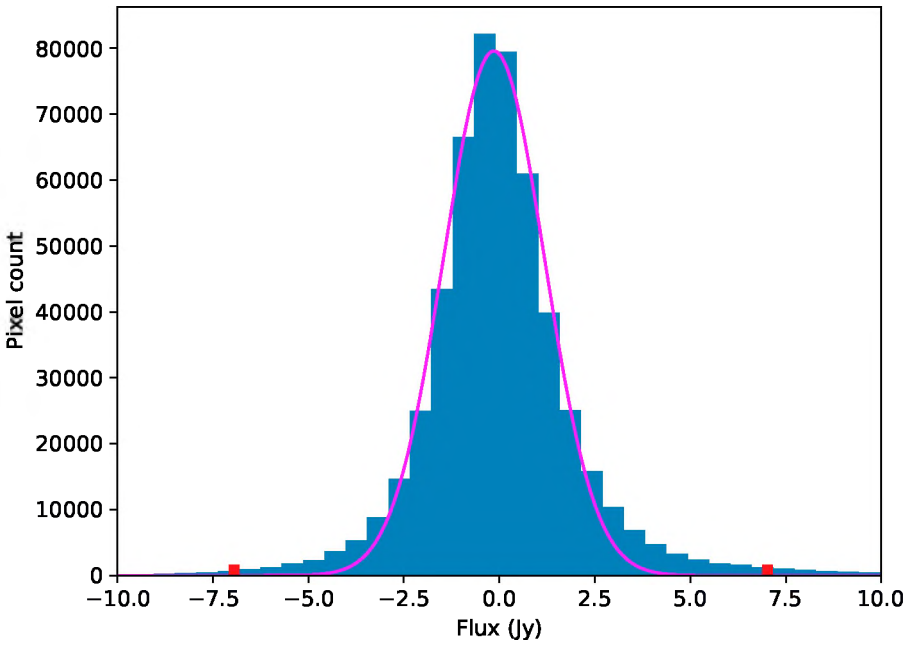

FIGURE 4.1: Pixel flux density distribution in the stacked LST = 10.8 hours image with a Gaussian distribution (magenta) fitted to the data (blue). The red square points give the range in which 98% of the pixels fall, which represents all the data within 3σ of the mean, μ.

We therefore proceeded to use the Python Blob Detection and Source Measurement (PyBDSM; Mohan & Rafferty, 2015) source finder software for our source extraction. The source extraction proceeds as follows:

- Noise characterization (or background estimation).

  The brightest pixels in the image are blanked in order to determine a first estimate of the image noise as the rms of the remaining pixels. This estimate is then refined by calculating the rms of sub-images defined by sliding a box car window across the whole image. If the rms values differ significantly across the image they are then used for the local source extraction, otherwise - like in our case - the average rms is taken as the constant noise across the image.

- Blob detection and thresholding.

  A blob (or island) is a group of contiguous pixels whose flux density is above a certain threshold and are a source candidate. In PyBDSM, this island threshold is specified as an integer number of the noise rms that is specified by the user: At least eight neighbouring pixels are required to be above the island threshold. At least one pixel out of eight needs to be brigther than a pixel threshold that is set

separately from the user to be another integer number of the rms noise. When both this conditions are satisfied, an island is then defined.

- Island parameterization.

  Sky sources are modeled within each island by fitting two dimensional Gaussians. For each pixel brighter than the pixels threshold, a Gaussian component is fitted. The best fit components are then subtracted from the image and another component search is performed. When no pixels brighter than the pixel threshold are present anymore, the fitted Gaussian components are combined into a single physical source.

We extracted sources from each individual LST-binned image (Figures 3.12, 3.13, 3.14, 3.15, 3.16 and 3.17) which have a $\sim 24'$ angular resolution. Although the LST bins have approximately the same observing time, the resulting image rms varies up to 50% across the LST range (Figure 4.2). This difference is caused by residual image artifacts due due to the presence of bright sources like Centaurus A or the Galactic centre. The most affected LST bin at 15.6 hours was indeed not used in the source extraction.

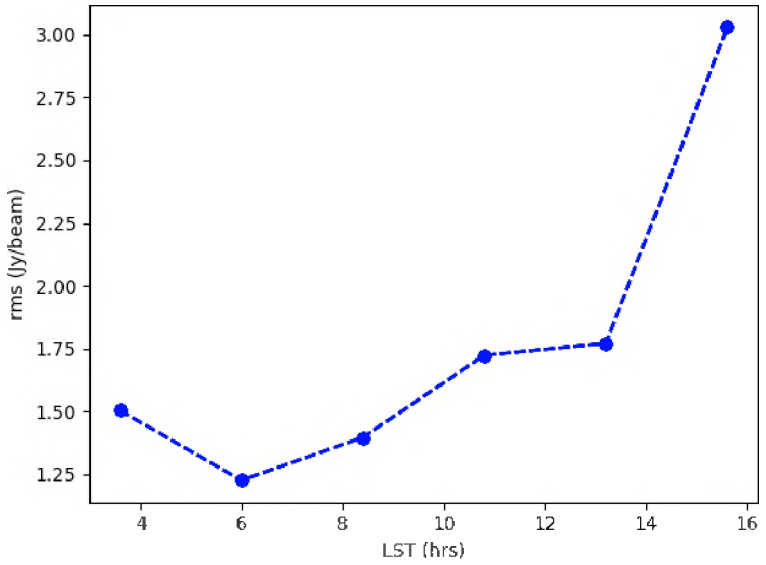

FIGURE 4.2: The background rms noise as a function of LST.

The island threshold selection was set to be five times the image rms noise - assumed constant across the image -, yelding a source flus density threshold of ~ 4 Jy. Figure 4.3 is an example of source extraction from the image centred at LST = 10.8 hours showing the islands identified as potential sources. We obtained such overlays for all the other maps, followed by a visual inspection in order to ensure that there are no false detections.

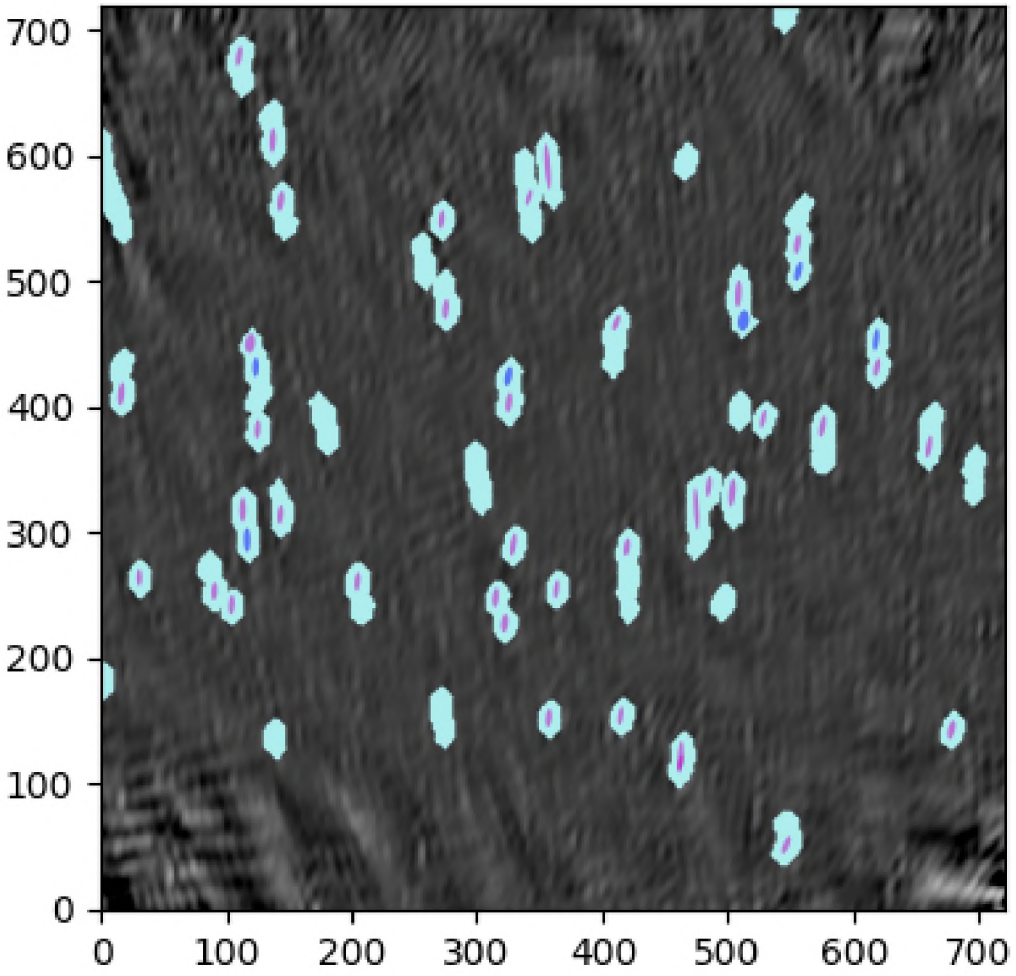

FIGURE 4.3: PyBDSM identifying potential sources for a LST=10.8 hours phased image. The cyan colour represents the blob extent while the pink colour represents pixels used in the Gaussian fit. The axis values represent pixel numbers.

We used again Pictor A to cross check the accuracy of the catalogue flux density. Figure 4.4 shows the Pictor A island identified by PyBDSM together with the pixels used in the actual Gaussian fit. The flux density obtained was 414 Jy, i.e. 9.1% brighter than the model (Jacobs et al., 2013). This value is consistent with the rms difference between our extracted Pictor A spectrum and the model (see Chapter 3). We corrected the flux density of the catalogue sources by this systematic offset.

Our catalogue includes 105 sources over a 4400 deg^2 area (see appendix). Bright sources excluded from the catalogue are Pictor A, Fornax A, Puppis A and Centaurus A. Simulations where point sources are injected in the visibility data or in the images are normally used to quantify the catalogue completeness. However, this exercise was not carried out in this work. As surveys normally approach completeness at the $6\sigma - 8\sigma$ level (Prandoni et al., 2001; Mauch et al., 2003; Hurley-Walker et al., 2014), we can consider our catalogue complete down to a ~ 8 Jy limit. Apart from the excluded bright

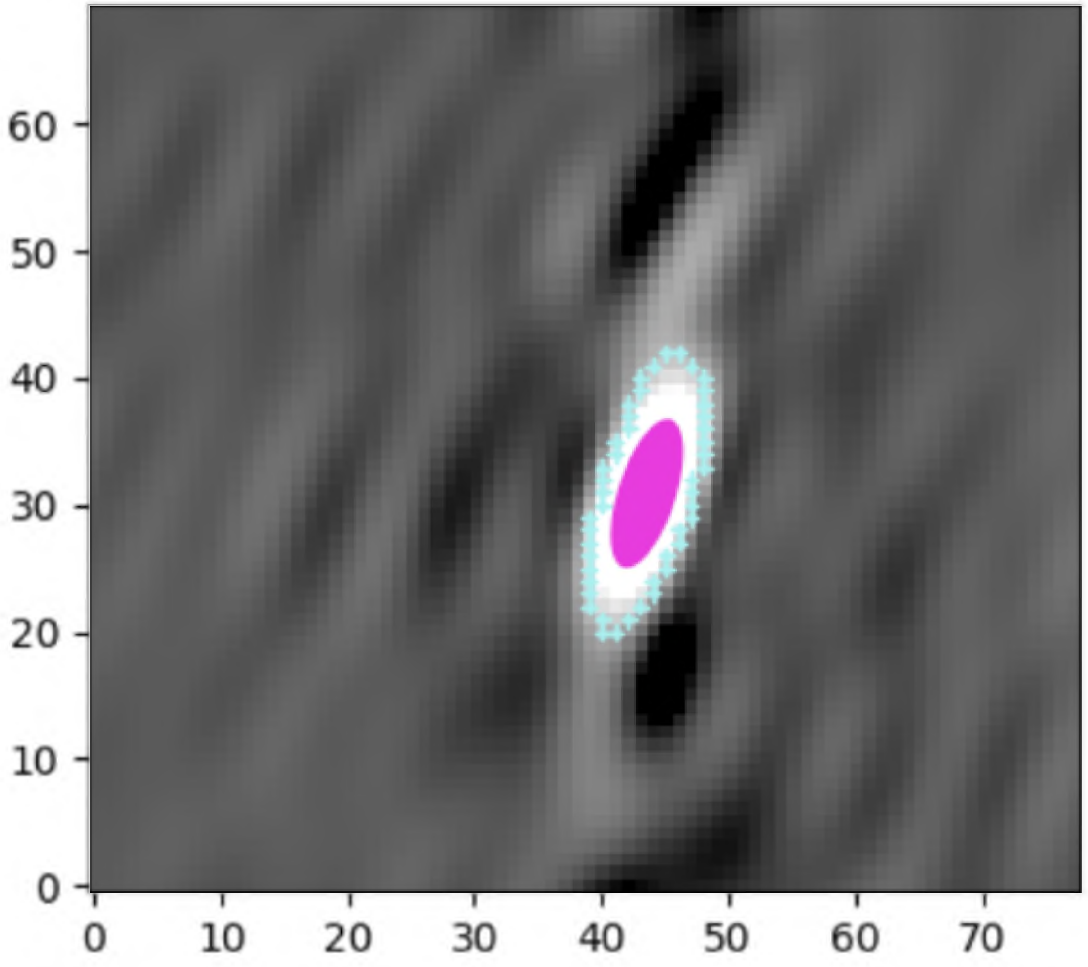

FIGURE 4.4: Source extraction using PyBDSM in the case of Pictor A. The cyan colour represents the blob extent while the pink colour represents pixels used in the Gaussian fit. The axis values are pixel numbers.

sources, the catalogue includes only sources that appear point-like at our resolution. We therefore included the peak flux density and the peak error in the catalogue rather than the integrated values.

4.2 Comparison with literature measurements

The best low frequency survey of the Southern sky to date is the GaLactic and ExtrA-galactic Meridian survey (GLEAM; Hurley-Walker et al., 2017). GLEAM covers the sky south of $\delta = 30°$ with almost continuous frequency coverage in the $70 - 230$ MHz range. With a ~ 2 arcmin resolution, it delivered a catalogue of ~ 300000 sources complete to a flux density limit of 160 mJy. We performed a comparison between our catalogue and the GLEAM one, bearing in mind that all the sources that we detected should be in the

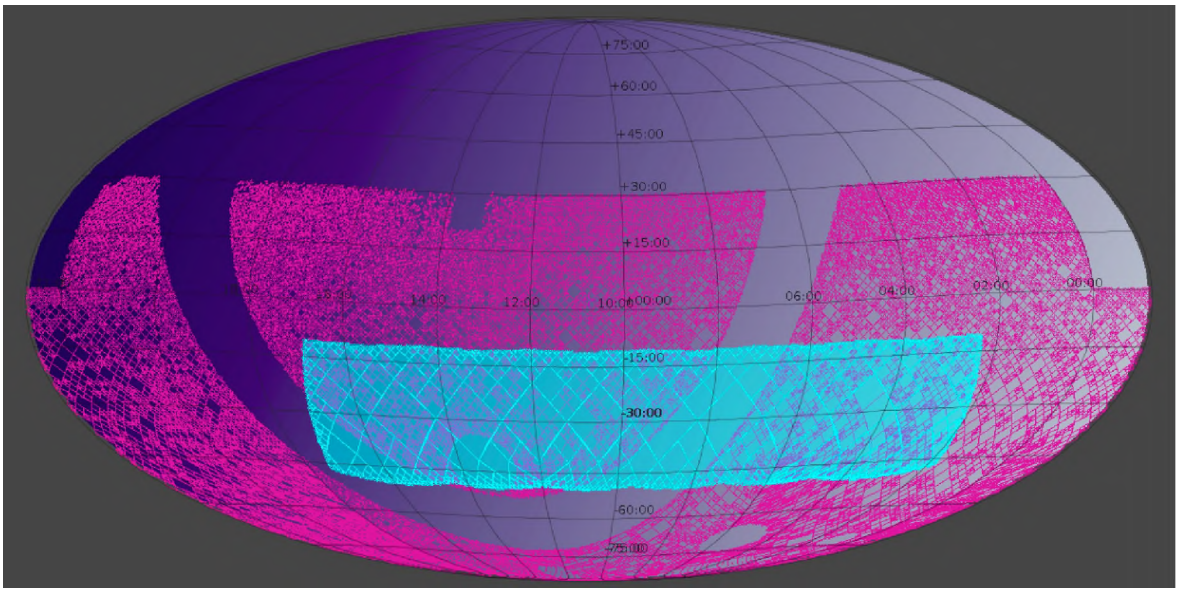

FIGURE 4.5: Multi-order coverage maps for GLEAM (magenta) and PAPER (cyan). The other regions represent sky areas which none of the two surveys cover. Parts of the galactic plane excluded by GLEAM can be seen to be covered by this PAPER survey as well as the very bright Centaurus A.

GLEAM catalogue since it is ≈ 90% complete at 0.16 Jy. We selected all the GLEAM sources brighter than 8 Jy, which is approximately the limit of our catalogue.

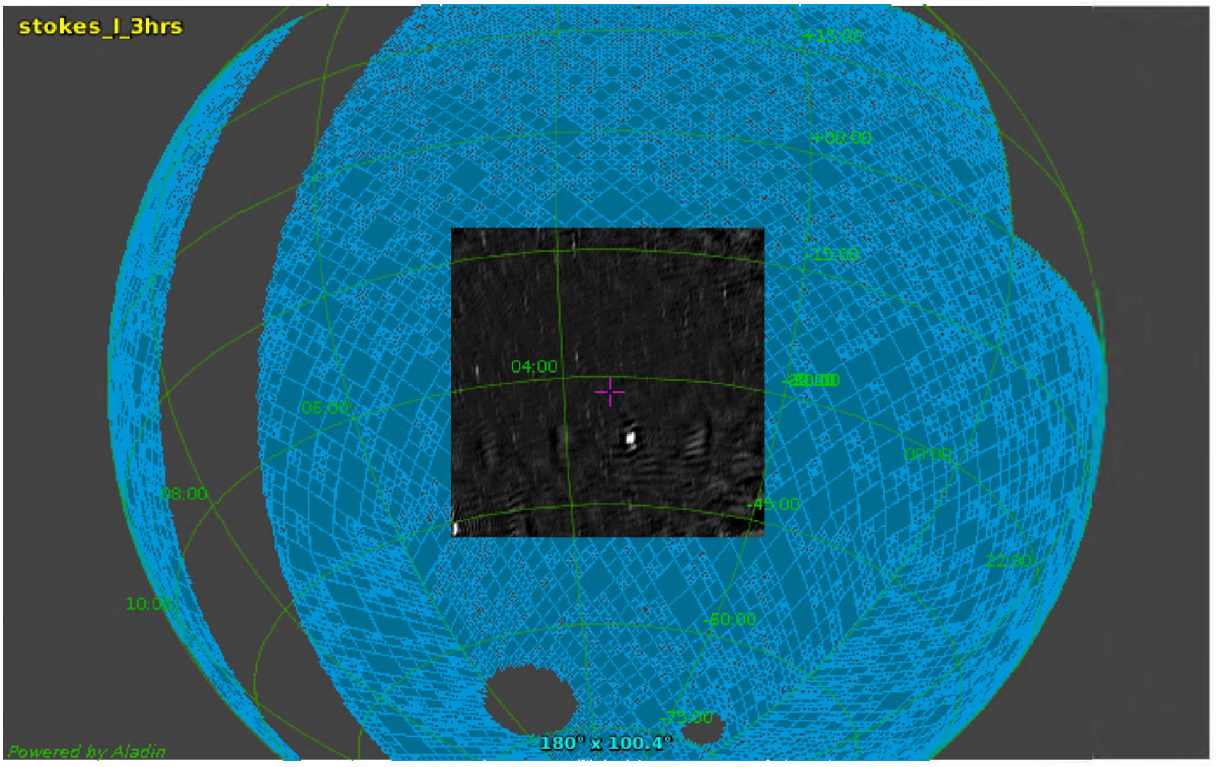

FIGURE 4.6: An animation at a frame per second, of the sky coverage of the GLEAM catalogue and PAPER sky maps obtained per LST bin. The GLEAM covers sky area south of +30° and excludes areas within 10° of the galactic plane.

Figure 4.5 and Figure 4.6 show the comparison between the GLEAM and PAPER sky coverages, whereas Figure 4.7 shows instead the GLEAM sources brighter than 8 Jy overlaid on the LST = 10.8 hours as an exaxmple. Although there are clearly fainter sources that remain without a GLEAM counterpart, all the bright GLEAM sources have a counterpart in the PAPER images, with a good position match. This result is common to each LST image analyzed.

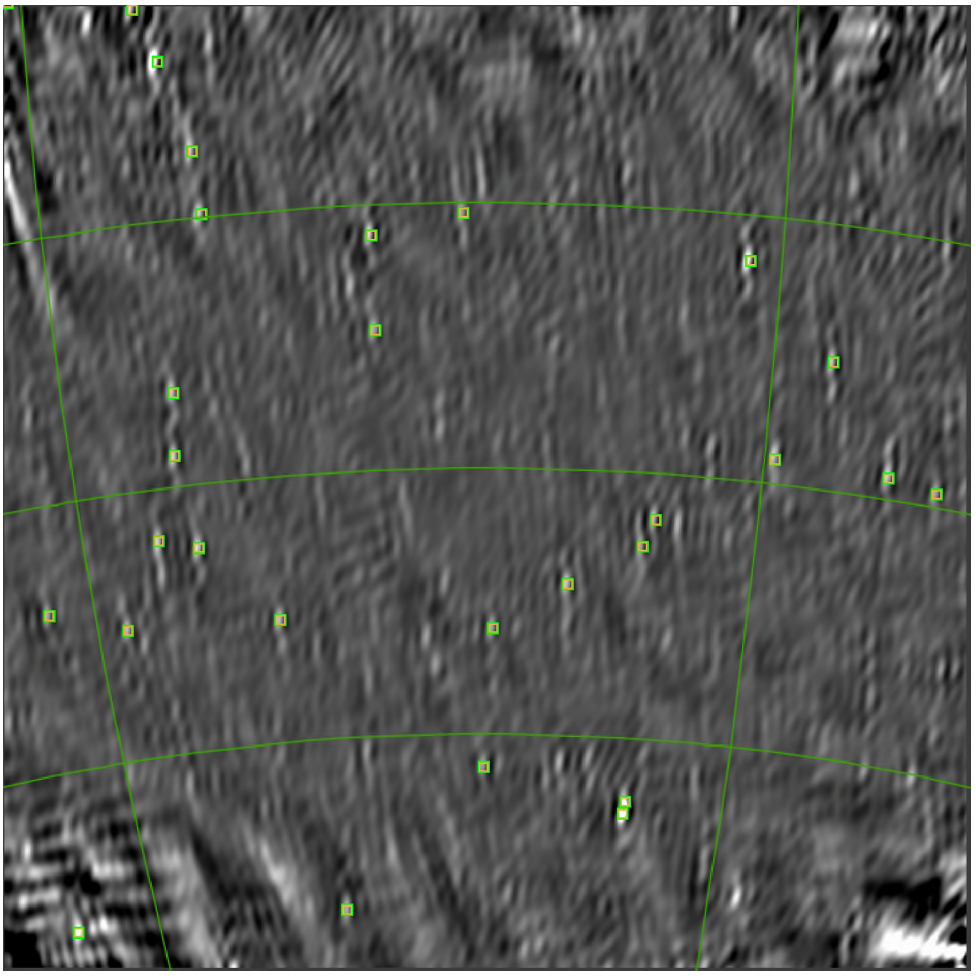

FIGURE 4.7: The LST = 10.8 hour image with sources from GLEAM brighter than 8 Jy overlaid. The bright spur in the bottom right corner is a region close to the galactic center and thus not covered by the GLEAM catalogue (see Figures 4.5 and 4.6).

In order to carry out a quantitative comparison, we matched each source to the closest GLEAM source within 15′ from the best fit position. In the cases listed below, we found that more than one GLEAM source was within 15′ from the best fit position:

- J063633-204225 matched four sources in the GLEAM catalogue;
- J070934-360349 and J040556-130645: they both have three different GLEAM sources.

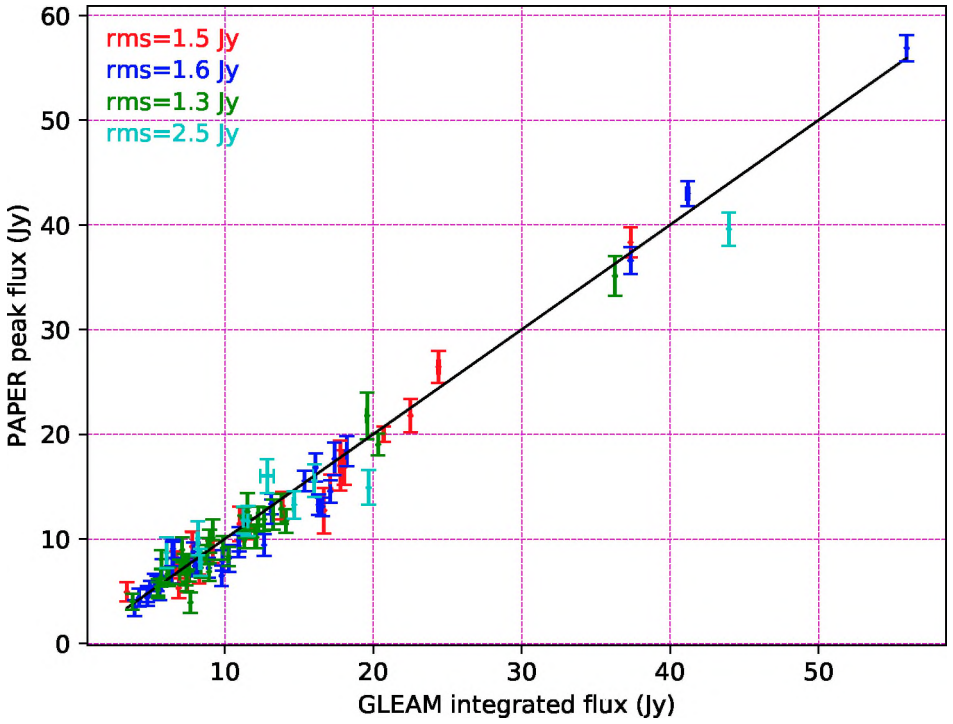

FIGURE 4.8: Comparison between the flux density scales between our survey and GLEAM. Different colours inidcate different LST images: 3.6 (red), 6.0 (blue), 10.8 (green), 13.2 (cyan) hours. The solid black line has the slope equals to one.

For these sources, the flux density from all the GLEAM sources was added together in the comparison. Figure 4.8 compares the flux densities for the common sources. We found a good agreement between the two flux scales, with no particular trend or bias and with a fractional difference rms better than 20% down to the $\sim$ 4 Jy limit. These results confirm the reliability of our absolute calibration over the survey area.

Ionospheric distortions were not corrected for in our calibration procedure. Although we expect their effect to be mild as our maximum baseline is only $\sim$ 335 m, our field of view is very wide and scintillation may occur for sources away from zenith. As ionospheric variation happens on scales smaller than our snapshot observations, sources could also be shifted from their intrinsic positions resulting in eventual positional errors in our final catalogue. Figure 4.9, 4.10 and 4.11 show that there is a 3.6 (1.2) arcmin mean offset in right ascension (declination) between the two catalogues. Positional difference remain within half of the synthesized beam size for any source. No particular trend is observed as a function of flux density other than the expected spread of positional differences as a function of decreasing flux density, although the source statistics remains limited. We did not have evidence to conclude that these offsets are due to ionospheric fluctuations, although this is a plausible explanation.

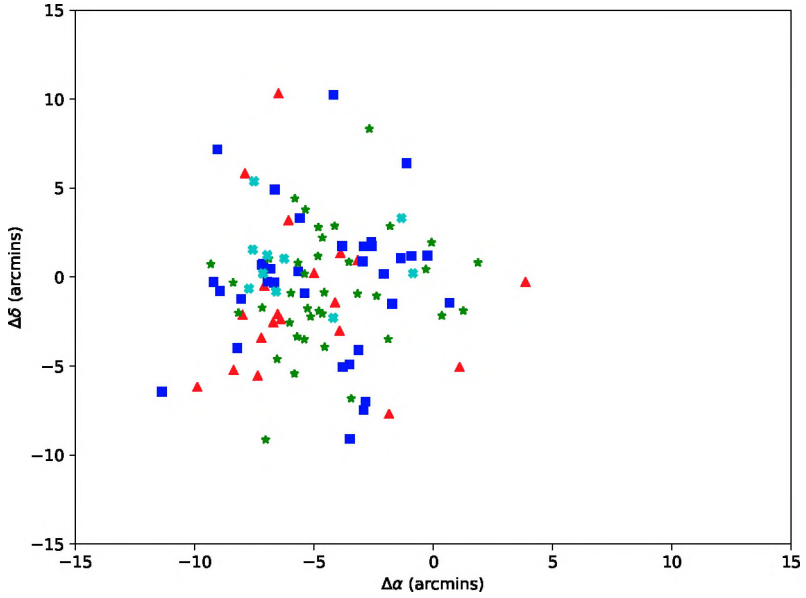

FIGURE 4.9: Positional difference between our catalogue and GLEAM one. The colour coding is the same as in Figure 4.8.

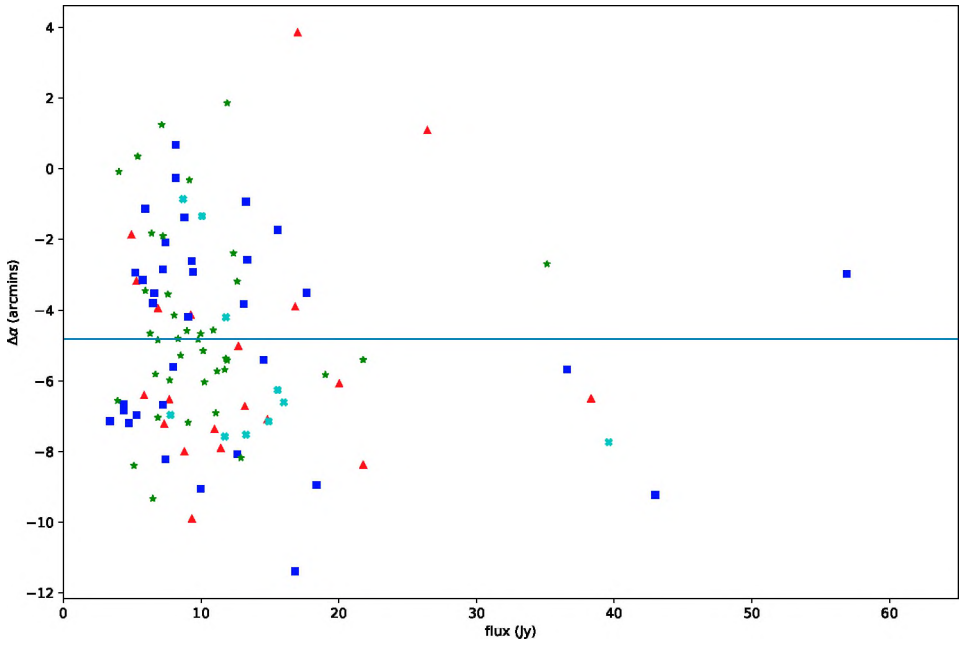

FIGURE 4.10: Right ascension positional offset as a function of source flux density. The blue solid line represents the median of the distribution while the points for 3.6, 6.0, 10.8 and 13.2 hours LST are shown by colours red, blue, green, and cyan respectively. The absolute mean value is 3.6 arcmin.

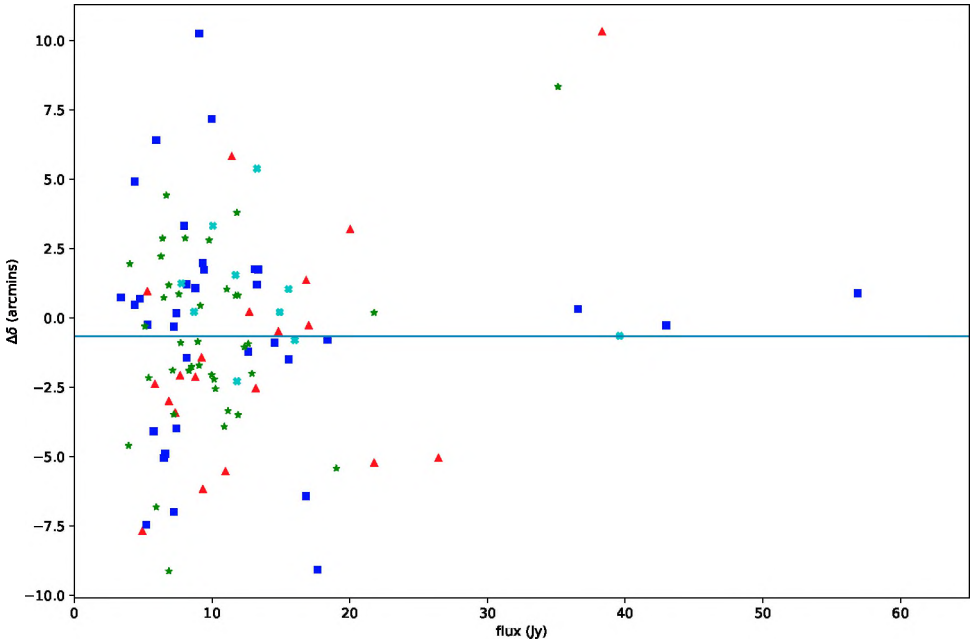

FIGURE 4.11: Same as Figure 4.10 but for the source declination. Colour coding is the same as in Figure 4.10. The absolute mean value is 1.2 arcmin.

Chapter 5

Conclusion

In this thesis, I have presented the analysis of 300 hours of observation with PAPER covering the $120 - 180$ MHz range. I took particular care in the absolute spectral calibration as this is relevant in order to measure the faint 21 cm signal from cosmic reionization - the main target of these observations. I did then proceed to generate images that cover the 7000 square degree sky area between $1^{\mathrm{h}}.8 < \alpha < 17^{\mathrm{h}}.4$ and $-10° > \delta > -48°$. In this process, I used an approach that is different from the standard interferometric imaging, motivated by the nature of the non-tracking array used, where individual snapshot images are combined together by primary beam weighting.

I then extracted a source catalogue, over an area of 4400 deg^2 from the images, that comprises of 105 sources, down to a 4 Jy flux density limit at 150 MHz. I validated the accuracy of the absolute flux density calibration against the existing GLEAM, finding a 19% fractional rms difference across the whole catalogue.

The catalogue offers confidence on the absolute spectral calibration and provides an all-sky accurate model of the extragalactic foreground to be used for the calibration of future observations and to be subtracted from the PAPER observations themselves in order to mitigate the foreground contamination.

Appendix A

Source Catalogue

The format of the final overall catalogue is as follows:

- Column 1 : Source name, taken from the GLEAM catalogue.
- Column 2 : The RA of the sources in J2000 coordinates.
- Column 3 : The DEC of the sources in J2000 coordinates.
- Column 4 : The source flux density at 150 MHz.
- Column 5 : The source spectral index from the GLEAM.

Source ID	α	δ	F (Jy)	β
J022343-281856	$02^h24^m02^s$	$-28°17'30''$	09.2 ± 1.4	-0.84
J023743-193232	$02^h38^m19^s$	$-19°27'18''$	21.8 ± 1.6	-0.71
J025616-261037	$02^h56^m25^s$	$-26°02'56''$	04.9 ± 0.9	-0.89
J025614-232447	$02^h56^m44^s$	$-23°22'15''$	13.1 ± 1.3	-0.99
J030731-222520	$03^h08^m06^s$	$-22°23'13''$	08.8 ± 1.1	-0.83
J031605-265906	$03^h16^m32^s$	$-26°55'29''$	05.9 ± 0.9	-1.16
J032123-451021	$03^h21^m15^s$	$-45°25'00''$	18.6 ± 2.3	-0.85
J033004-163847	$03^h30^m46^s$	$-16°32'37''$	09.3 ± 1.3	-0.96
J034631-342238	$03^h46^m55^s$	$-34°22'51''$	12.7 ± 2.1	-0.74
J035140-274354	$03^h52^m07^s$	$-27°43'14''$	20.0 ± 0.7	-0.80
J035129-142923	$03^h52^m13^s$	$-14°29'53''$	26.4 ± 1.5	-0.97
J040534-130813	$04^h06^m24^s$	$-13°11'01''$	11.4 ± 1.6	-0.84
J040851-241817	$04^h09^m22^s$	$-24°14'53''$	07.3 ± 0.7	-1.07
J040906-175708	$04^h09^m43^s$	$-17°58'39''$	07.7 ± 1.1	-0.94
J041508-292901	$04^h15^m27^s$	$-29°26'01''$	06.7 ± 1.1	-0.95

J041604-205627	$04^{\mathrm{h}}16^{\mathrm{m}}36^{\mathrm{s}}$	$-20°50'56''$	10.9 ± 0.9	-0.98
J042940-363050	$04^{\mathrm{h}}29^{\mathrm{m}}58^{\mathrm{s}}$	$-36°21'45''$	17.6 ± 1.5	-0.87
J043415-131030	$04^{\mathrm{h}}34^{\mathrm{m}}54^{\mathrm{s}}$	$-13°11'19''$	16.8 ± 1.6	-0.75
J044437-280948	$04^{\mathrm{h}}45^{\mathrm{m}}03^{\mathrm{s}}$	$-28°10'08''$	36.6 ± 1.3	-0.76
J044437-280948	$04^{\mathrm{h}}45^{\mathrm{m}}07^{\mathrm{s}}$	$-28°20'08''$	32.1 ± 1.4	-0.76
J044829-203217	$04^{\mathrm{h}}49^{\mathrm{m}}02^{\mathrm{s}}$	$-20°32'57''$	08.1 ± 1.5	-0.93
J045514-300646	$04^{\mathrm{h}}55^{\mathrm{m}}47^{\mathrm{s}}$	$-30°06'17''$	14.8 ± 1.3	-0.78
J045523-203413	$04^{\mathrm{h}}56^{\mathrm{m}}00^{\mathrm{s}}$	$-20°26'12''$	16.8 ± 1.3	-0.60
J045610-215922	$04^{\mathrm{h}}56^{\mathrm{m}}41^{\mathrm{s}}$	$-22°01'43''$	08.1 ± 1.3	-0.78
J045826-300717	$04^{\mathrm{h}}58^{\mathrm{m}}40^{\mathrm{s}}$	$-30°09'01''$	09.4 ± 1.0	-0.79
J050539-282627	$05^{\mathrm{h}}06^{\mathrm{m}}01^{\mathrm{s}}$	$-28°34'46''$	09.1 ± 0.8	-0.81
J051032-183843	$05^{\mathrm{h}}11^{\mathrm{m}}10^{\mathrm{s}}$	$-18°37'56''$	18.3 ± 1.4	-1.29
J051100-220153	$05^{\mathrm{h}}11^{\mathrm{m}}36^{\mathrm{s}}$	$-21°57'54''$	07.4 ± 0.9	-0.70
J051329-303042	$05^{\mathrm{h}}14^{\mathrm{m}}00^{\mathrm{s}}$	$-30°26'36''$	13.2 ± 0.9	-0.77
J052139-204737	$05^{\mathrm{h}}22^{\mathrm{m}}13^{\mathrm{s}}$	$-20°46'24''$	12.6 ± 1.1	-0.61
J052257-362727	$05^{\mathrm{h}}23^{\mathrm{m}}13^{\mathrm{s}}$	$-36°28'20''$	56.9 ± 1.2	-0.61
J053115-303210	$05^{\mathrm{h}}31^{\mathrm{m}}46^{\mathrm{s}}$	$-30°37'06''$	04.4 ± 8.8	-0.84
J053949-341235	$05^{\mathrm{h}}40^{\mathrm{m}}06^{\mathrm{s}}$	$-34°07'41''$	06.5 ± 0.8	-0.94
J054307-242103	$05^{\mathrm{h}}43^{\mathrm{m}}42^{\mathrm{s}}$	$-24°19'59''$	07.4 ± 0.7	-0.96
J054558-263015	$05^{\mathrm{h}}46^{\mathrm{m}}24^{\mathrm{s}}$	$-26°26'29''$	04.7 ± 0.8	-0.73
J054617-172548	$05^{\mathrm{h}}46^{\mathrm{m}}51^{\mathrm{s}}$	$-17°17'26''$	05.2 ± 1.0	-0.75
J054924-405110	$05^{\mathrm{h}}49^{\mathrm{m}}33^{\mathrm{s}}$	$-40°49'40''$	15.5 ± 0.9	-0.81
J045514-300646	$05^{\mathrm{h}}55^{\mathrm{m}}39^{\mathrm{s}}$	$-30°05'52''$	14.5 ± 1.1	-0.78
J055759-285546	$05^{\mathrm{h}}58^{\mathrm{m}}24^{\mathrm{s}}$	$-29°01'03''$	05.7 ± 0.7	-0.56
J055820-280912	$05^{\mathrm{h}}58^{\mathrm{m}}53^{\mathrm{s}}$	$-28°06'14''$	05.9 ± 0.7	-0.89
J060101-392612	$06^{\mathrm{h}}01^{\mathrm{m}}15^{\mathrm{s}}$	$-39°19'13''$	07.2 ± 0.8	-1.06
J060203-381905	$06^{\mathrm{h}}02^{\mathrm{m}}10^{\mathrm{s}}$	$-38°17'23''$	08.7 ± 0.9	-0.94
J060312-342632	$06^{\mathrm{h}}03^{\mathrm{m}}31^{\mathrm{s}}$	$-34°21'29''$	06.5 ± 0.9	-0.95
J060414-315555	$06^{\mathrm{h}}04^{\mathrm{m}}46^{\mathrm{s}}$	$-31°55'36''$	07.2 ± 0.9	-0.66
J060634-202157	$06^{\mathrm{h}}07^{\mathrm{m}}13^{\mathrm{s}}$	$-20°29'08''$	10.0 ± 1.2	-0.58
J061334-253038	$06^{\mathrm{h}}14^{\mathrm{m}}02^{\mathrm{s}}$	$-25°25'31''$	04.4 ± 0.8	-0.74
J061721-282547	$06^{\mathrm{h}}17^{\mathrm{m}}52^{\mathrm{s}}$	$-28°25'32''$	05.3 ± 0.7	-0.98
J062000-371133	$06^{\mathrm{h}}20^{\mathrm{m}}29^{\mathrm{s}}$	$-37°14'52''$	08.0 ± 0.9	-0.71
J062707-352908	$06^{\mathrm{h}}27^{\mathrm{m}}26^{\mathrm{s}}$	$-35°30'53''$	13.1 ± 0.9	-0.73
J063633-204225	$06^{\mathrm{h}}37^{\mathrm{m}}11^{\mathrm{s}}$	$-20°35'10''$	43.0 ± 1.2	-0.76
J063858-283814	$06^{\mathrm{h}}39^{\mathrm{m}}43^{\mathrm{s}}$	$-28°37'14''$	03.4 ± 0.8	-0.64
J064811-395704	$06^{\mathrm{h}}48^{\mathrm{m}}25^{\mathrm{s}}$	$-39°58'49''$	13.3 ± 1.0	-0.91
J070934-360341	$07^{\mathrm{h}}09^{\mathrm{m}}43^{\mathrm{s}}$	$-36°02'19''$	17.0 ± 2.3	-0.85
J082717-202619	$08^{\mathrm{h}}27^{\mathrm{m}}57^{\mathrm{s}}$	$-20°27'12''$	19.5 ± 1.1	-0.44

J090147-255516	$09^{\rm h}02^{\rm m}21^{\rm s}$	$-25°54'52''$	27.0 ± 1.2	-0.68
J092902-293017	$09^{\rm h}29^{\rm m}21^{\rm s}$	$-29°32'16''$	07.3 ± 1.4	-0.95
J092902-293017	$09^{\rm h}29^{\rm m}30^{\rm s}$	$-29°29'24''$	07.6 ± 0.6	-0.95
J093800-291244	$09^{\rm h}38^{\rm m}19^{\rm s}$	$-29°08'34''$	11.9 ± 1.2	-0.86
J094953-251138	$09^{\rm h}50^{\rm m}24^{\rm s}$	$-25°12'40''$	11.1 ± 0.9	-0.93
J095804-290408	$09^{\rm h}58^{\rm m}30^{\rm s}$	$-28°54'39''$	10.9 ± 0.9	-0.89
J100511-214451	$10^{\rm h}05^{\rm m}44^{\rm s}$	$-21°44'04''$	19.0 ± 1.1	-1.07
J100910-285552	$10^{\rm h}09^{\rm m}30^{\rm s}$	$-28°50'27''$	07.6 ± 0.9	-0.64
J101348-315323	$10^{\rm h}14^{\rm m}10^{\rm s}$	$-31°52'32''$	08.9 ± 1.2	-0.79
J101503-235705	$10^{\rm h}15^{\rm m}31^{\rm s}$	$-23°56'31''$	05.4 ± 0.8	-0.99
J101809-314411	$10^{\rm h}18^{\rm m}37^{\rm s}$	$-31°41'38''$	10.2 ± 1.1	-0.48
J102003-425130	$10^{\rm h}20^{\rm m}09^{\rm s}$	$-42°44'24''$	35.1 ± 1.9	-0.83
J102011-324533	$10^{\rm h}20^{\rm m}45^{\rm s}$	$-32°36'25''$	06.8 ± 0.9	-0.79
J103327-410814	$10^{\rm h}33^{\rm m}34^{\rm s}$	$-41°02'20''$	09.1 ± 1.1	-1.02
J103312-341842	$10^{\rm h}33^{\rm m}37^{\rm s}$	$-34°16'29''$	10.2 ± 1.0	-0.95
J103611-252516	$10^{\rm h}36^{\rm m}43^{\rm s}$	$-25°19'53''$	04.0 ± 0.7	-0.88
J104645-360126	$10^{\rm h}47^{\rm m}11^{\rm s}$	$-35°59'41''$	08.5 ± 0.9	-0.88
J104837-411352	$10^{\rm h}48^{\rm m}48^{\rm s}$	$-41°10'23''$	07.2 ± 0.9	-0.81
J104807-190935	$10^{\rm h}48^{\rm m}50^{\rm s}$	$-19°04'22''$	08.1 ± 0.9	-0.87
J105132-202344	$10^{\rm h}52^{\rm m}00^{\rm s}$	$-20°19'08''$	03.9 ± 1.0	-0.61
J105514-341855	$10^{\rm h}55^{\rm m}30^{\rm s}$	$-34°12'06''$	05.9 ± 0.9	-0.96
J105516-272950	$10^{\rm h}55^{\rm m}54^{\rm s}$	$-27°29'32''$	05.1 ± 0.8	-1.09
J105533-283134	$10^{\rm h}55^{\rm m}54^{\rm s}$	$-28°32'17''$	06.5 ± 0.7	-0.64
J105709-371833	$10^{\rm h}57^{\rm m}34^{\rm s}$	$-37°19'45''$	06.8 ± 1.2	-0.76
J105854-362051	$10^{\rm h}59^{\rm m}11^{\rm s}$	$-36°18'20''$	07.1 ± 1.2	-0.75
J110611-244443	$11^{\rm h}06^{\rm m}43^{\rm s}$	$-24°43'00''$	09.0 ± 1.1	-1.01
J110622-210859	$11^{\rm h}06^{\rm m}57^{\rm s}$	$-21°06'59''$	12.9 ± 1.4	-0.74
J111119-403043	$11^{\rm h}11^{\rm m}43^{\rm s}$	$-40°32'56''$	06.3 ± 0.8	-0.71
J112554-352321	$11^{\rm h}26^{\rm m}17^{\rm s}$	$-35°21'18''$	10.0 ± 0.9	-0.72
J113336-195415	$11^{\rm h}34^{\rm m}17^{\rm s}$	$-19°53'47''$	12.3 ± 1.4	-0.86
J113423-172750	$11^{\rm h}35^{\rm m}02^{\rm s}$	$-17°23'49''$	12.6 ± 1.7	-0.81
J113917-322237	$11^{\rm h}39^{\rm m}44^{\rm s}$	$-17°23'25''$	11.7 ± 1.1	-0.88
J113910-135044	$11^{\rm h}39^{\rm m}47^{\rm s}$	$-13°46'36''$	21.8 ± 2.2	-0.78
J114048-262908	$11^{\rm h}41^{\rm m}14^{\rm s}$	$-26°25'47''$	11.1 ± 1.1	-1.15
J114134-285050	$11^{\rm h}42^{\rm m}07^{\rm s}$	$-28°54'10''$	11.9 ± 1.1	-0.70
J114628-332838	$11^{\rm h}46^{\rm m}36^{\rm s}$	$-33°23'06''$	10.1 ± 1.6	-0.69
J114620-315713	$11^{\rm h}46^{\rm m}40^{\rm s}$	$-31°54'56''$	11.8 ± 1.3	-0.91
J114620-315713	$11^{\rm h}46^{\rm m}46^{\rm s}$	$-32°01'01''$	11.8 ± 1.2	-0.91
J115115-353701	$11^{\rm h}51^{\rm m}43^{\rm s}$	$-35°41'27''$	06.7 ± 1.1	-0.82

J115421-350525	$11^{\mathrm{h}}54^{\mathrm{m}}43^{\mathrm{s}}$	$-35°03'57''$	09.8 ± 1.1	$+0.31$
J120533-263407	$12^{\mathrm{h}}06^{\mathrm{m}}21^{\mathrm{s}}$	$-26°41'08''$	06.4 ± 0.8	-0.77
J120839-340306	$12^{\mathrm{h}}09^{\mathrm{m}}02^{\mathrm{s}}$	$-34°01'12''$	08.3 ± 0.9	-0.93
J125441-291343	$12^{\mathrm{h}}55^{\mathrm{m}}06^{\mathrm{s}}$	$-29°14'39''$	13.2 ± 1.3	-1.19
J131139-221640	$13^{\mathrm{h}}12^{\mathrm{m}}13^{\mathrm{s}}$	$-22°16'02''$	39.6 ± 1.6	-0.55
J133007-214203	$13^{\mathrm{h}}30^{\mathrm{m}}40^{\mathrm{s}}$	$-21°43'36''$	11.7 ± 1.4	-0.94
J133659-295147	$13^{\mathrm{h}}37^{\mathrm{m}}32^{\mathrm{s}}$	$-29°53'02''$	07.8 ± 1.3	-0.68
J140421-340018	$14^{\mathrm{h}}04^{\mathrm{m}}30^{\mathrm{s}}$	$-34°04'07''$	16.0 ± 1.6	-1.31
J140459-253537	$14^{\mathrm{h}}05^{\mathrm{m}}15^{\mathrm{s}}$	$-25°30'23''$	08.6 ± 1.5	-0.87
J142249-272755	$14^{\mathrm{h}}23^{\mathrm{m}}21^{\mathrm{s}}$	$-27°28'07''$	14.9 ± 1.6	-0.98
J142529-295955	$14^{\mathrm{h}}25^{\mathrm{m}}58^{\mathrm{s}}$	$-30°00'57''$	15.5 ± 1.6	-0.90

Bibliography

Abel T., Bryan G. L., Norman M. L., 2002, Science, 295, 93

Adam R., et al., 2016, A&A, 596, A108

Aghanim N., Majumdar S., Silk J., 2008, Reports Prog. Phys., 71, 66902

Ali Z., Parsons A., Zheng H., Pober J., Liu A., Aguirre J., Bradley R., Bernardi G., et al., 2015, ApJ, 809, 61

Barkana R., 2018, Nature, 555, 71

Barkana R., Loeb A., 2001, Phys. Rep., 349, 125

Beardsley A. P., Hazelton B. J., Sullivan I. S., Carroll P., Barry N., Rahimi M., Pindor B., et al., 2016, The Astrophysical Journal, 833, 102

Becker G. D., Bolton J. S., Lidz A., 2015, Publ. Astron. Soc. Austral., 32, e045

Bennett C. L., Larson D., Weiland J. L., Jarosik N., Hinshaw G., Odegard N., Smith K. M., et al., 2013, ApJS, 208, 20

Bernardi G., de Bruyn, A. G. Brentjens, M. A. Ciardi, B. Harker, G. et al., 2009, A&A, 500, 965

Bernardi G., Greenhill L. J., Mitchell D. A., Ord S. M., Hazelton B. J., et al., 2013, ApJ, 771, 105

Bernardi G., Mitchell D., Ord S., Greenhill L., Pindor B., Wayth R., Wyithe J., et al., 2010, MNRAS, 413, 411

Beuermann K., Kanbach G., Berkhuijsen E. M., 1985, AAP, 153, 17

Bobin J., Starck J.-L., Fadili J., Moudden Y., 2007, IEEE Transactions on Image Processing, 16, 2662

Bouwens R. J., Illingworth G. D., Oesch P. A., Trenti M., Labbé I., Bradley L., Carollo M., et al., 2015, ApJ, 803, 1

Bowman J. D., Cairns I., Kaplan D. L., Murphy T., Oberoi D., et al., 2013, Publ. Astron. Soc. Aust., 30

Bowman J. D., Morales M. F., Hewitt J. N., et al., 2009, ApJ, 695, 183

Bowman J. D., Rogers A. E., Monsalve R. A., Mozdzen T. J., Mahesh N., 2018, Nature, 555, 67

Bowman J. D., Rogers A. E. E., 2010, Nature, 468, 796

Bromm V., Larson R. B., 2004, Ann. Rev. Astron. Astrophys., 42, 79

Callingham J. R., Ekers R. D., Gaensler B. M., Line J. L. B., Hurley-Walker N., Sadler E. M., Tingay S. J., et al., 2017, ApJ, 836, 174

Carroll B., Ostlie D., 2007, An Introduction to Modern Astrophysics. Pearson Addison-Wesley

Caruana J., Bunker A. J., Wilkins S. M., Stanway E. R., Lacy M., Jarvis M. J., Lorenzoni S., Hickey S., 2012, MNRAS, 427, 3055

Chapman E., Abdalla F. B., Bobin J., Starck J.-L., Harker G., Jelić V., Labropoulos P., et al., 2013, Monthly Notices of the Royal Astronomical Society, 429, 165

Chapman E., Zaroubi S., Abdalla F. B., Dulwich F., Jelić V., Mort B., et al., 2016, MNRAS, 458, 2928

Cheng C., Parsons A. R., Kolopanis M., Jacobs D. C., Liu A., Kohn S. A., Aguirre J. E., et al., 2018, ApJ, 868, 26

Cohen A. S., Rottgering H. J. A., Jarvis M. J., Kassim N. E., Lazio T. J. W., 2004, ApJS, 150, 417

Cornwell T., Golap K., Bhatnagar S., 2008, IEEE J. Sel. Top. Signal Process., 2, 647

Datta A., Bowman J. D., Carilli C. L., 2010, ApJ, 724, 526

Deboer D. R., Parsons A. R., Aguirre J. E., Alexander P., Ali Z. S., et al., 2017, Publ. Astron. Soc. Pacific, 129

Di Matteo T., Perna R., Abel T., Rees M. J., 2002, ApJ, 564, 576

Dicke R. H., Peebles P. J. E., Roll P. G., Wilkinson D. T., 1965, ApJ, 142, 414

Dijkstra M., Mesinger A., Wyithe J. S. B., 2011, MNRAS, 414, 2139

Dijkstra M., Wyithe J. S. B., 2012, Monthly Notices of the Royal Astronomical Society, 419, 3181

Dillon J. S., Liu A., Williams C. L., Hewitt J. N., Tegmark M., Morgan E. H., Levine A. M., et al., 2014, prd, 89, 023002

Dillon J. S., Tegmark M., Liu A., Ewall-Wice A., Hewitt J. N., Morales M. F., Neben A. R., et al., 2015, prd, 91, 023002

Ewen. Purcell. 1951, Nature, 168

Fan X.-H., Carilli C. L., Keating B. G., 2006, Ann. Rev. Astron. Astrophys., 44, 415

Fan X.-H., Strauss M. A., Becker R. H., White R. L., Gunn J. E., Knapp G. R., Richards G. T., et al., 2006, Astron. J., 132, 117

Field G. B., 1959, ApJ, 129, 536

Franzen T. M. O., Jackson C. A., Offringa A. R., Ekers R. D., Wayth R. B., Bernardi G., Bowman J. D., et al., 2016, MNRAS, 459, 3314

Frebel A., Johnson J. L., Bromm V., 2007, MNRAS, 380, L40

Furlanetto S. R., Furlanetto M. R., 2007, MNRAS, 374, 547

Furlanetto S. R., Oh S. P., Briggs F. H., 2006, physrep, 433, 181

George E. M., et al., 2014, ApJ, 799, 177

Greig B., Mesinger A., 2017, MNRAS, 465, 4838

Gunn J. E., Peterson B. A., 1965, ApJ, 142, 1633

Guth A. H., 1981, Phys. Rev. D, 23, 347

Hales S. E. G., Baldwin J. E., Warner P. J., 1988, MNRAS, 234, 919

Harker G., Zaroubi S., Bernardi G., Brentjens M. A., De Bruyn A. G., Ciardi B., Jelić V., et al., 2009, MNRAS, 397, 1138

Harker G., Zaroubi S., Bernardi G., Brentjens M. A., de Bruyn A. G., Ciardi B., Jelić V., et al., 2010, MNRAS, 405, 2492

Haslam C. G. T., Salter C. J., Stoffel H., Wilson W. E., 1982, AAPS, 47, 1

Haverkorn M., Katgert P., de Bruyn A. G., 2003a, AAp, 403, 1045

Haverkorn M., Katgert P., de Bruyn A. G., 2003b, AAP, 404, 233

Heald G. H., Pizzo R. F., Orrú E., Breton R. P., Carbone D., Ferrari C., et al., 2015, A&A, 582, 123

Hills R., Kulkarni G., Meerburg P. D., Puchwein E., 2018, arXiv e-prints, p. arXiv:1805.01421

Hinshaw G., Larson D., Komatsu E., Spergel D. N., Bennett C. L., Dunkley J., Nolta M. R., et al., 2013, ApJS, 208, 19

Hopkins A. M., Miller C. J., Connolly A. J., Genovese C., Nichol R. C., et al., 2002, AJ, 123, 1086

Hu E. M., Cowie L. L., Barger A. J., Capak P., Kakazu Y., Trouille L., 2010, ApJ, 725, 394

Hu W., White M., 1997, New Astron., 2, 323

Hurley-Walker N., Callingham J. R., Hancock P. J., Franzen T. M., et al., 2017, MNRAS, 464, 1146

Hurley-Walker N., Morgan J., Wayth R. B., Hancock P. J., et al., 2014, Publ. Astron. Soc. Aust., 31

Huynh M. T., Hopkins A. M., Lenc E., Mao M. Y., Middelberg E., Norris R. P., Randall K. E. a., 2012, MNRAS, 426, 2342

Iliev I. T., Mellema G., Pen U. L., Merz H., Shapiro P. R., Alvarez M. A., 2006, MNRAS, 369, 1625

Intema H. T., van Weeren R. J., Röttgering H. J. A., Lal D. V., 2011, AAP, 535, A38

Jacobs D. C., Parsons A. R., Aguirre J. E., Ali Z., Bowman J., Bradley R. F., Carilli C. L., et al., 2013, ApJ, 776, 108

Jensen H., Laursen P., Mellema G., Iliev I. T., Sommer-Larsen J., Shapiro P. R., et al., 2013, MNRAS, 428, 1366

Jordan C. H., Murray S., Trott C. M., Wayth R. B., Mitchell D. A., Rahimi M., Pindor B., et al., 2017, MNRAS, 14, 1

Kaiser N., 1987, MNRAS, 227, 1

Kashikawa N., Yoshida M., Shimasaku K., 2006, ApJ, 637, 631

Kerrigan J. R., Pober J. C., Ali Z. S., Cheng C., Beardsley A. P., Parsons A. R., Aguirre J. E., et al., 2018, ApJ, 864, 131

Kohn S., Aguirre J., Nunhokee C., Bernardi G., Pober J., Ali Z., Bradley R., et al., 2016, ApJ, 823, 88

Kohn S., Chichura P. M., Igarashi A. S., Fortino A. F., Aguirre J. E., Benefo R. K., Billings T. S., et al., 2018, ArXiv e-prints

Lidz A., Zahn O., McQuinn M., Zaldarriaga M., Hernquist L., 2008, ApJ, 680, 962

Liju P., 2016, Master's thesis, Rhodes University

Linde A. D., 1982, Phys. Lett., 108B, 389

Liu A., Tegmark M., Bowman J., Hewitt J., Zaldarriaga M., 2009, MNRAS, 398, 401

Liu A., Tegmark M., Morrison S., Lutomirski A., Zaldarriaga M., 2010, MNRAS, 408, 1029

Loeb A., 2010, How Did the First Stars and Galaxies Form?. Princeton frontiers in physics, Princeton University Press

Loi S. T., Trott C. M., Murphy T., Cairns I. H., Bell M., H N., et al., 2015, Radio Sci., 50, 574

Longair M. S., 2011, High Energy Astrophysics, 3rd edn., by Malcolm S. Longair. UK: Cambridge University Press

Mclure R. J., Dunlop J. S., de Ravel L., Cirasuolo M., Ellis R. S., Schenker M., Robertson B. E., et al., 2011, MNRAS, 418, 2074

Mahony E., Morganti R., Prandoni I., M. van Bemmel I., W. Shimwell T., Brienza M., et al., 2016, MNRAS, 463

Malhotra S., Rhoads J. E., 2004, ApJl, 617, L5

Mather J. C., Cheng E. S., Cottingham D. A., Eplee, R. E. J., Fixsen D. J., Hewagama T., et al., 1994, ApJ, 420, 439

Mauch T., Murphy T., Buttery H. J., Curran J., Hunstead R. W., Piestrzynski B., Robertson J. G., et al., 2003, MNRAS, 342, 1117

McQuinn M., Lidz A., Zahn O., Dutta S., Hernquist L., Zaldarriaga M., 2007, MNRAS, 377, 1043

Mellema G., Iliev I. T., Pen U. L., Shapiro P. R., et al., 2006, MNRAS, 372, 679

Mesinger A., Ferrara A., Greig B., Iliev I., Mellema G., Pritchard J., Santos M. G., 2015, PoS, AASKA14, 011

Mesinger A., Furlanetto S., Cen R., 2011, MNRAS, 411, 955

Mevius M., van der Tol S., Pandey V. N., Vedantham H. K., et al., 2016, Radio Sci., 51, 927

Mitchell D. A., Greenhill L. J., Wayth R. B., Sault R. J., Lonsdale C. J., Cappallo R. J., Morales M. F., Ord S. M., et al., 2008, IEEE J. Sel. Top. Signal Process., 2, 707

Mohan N., Rafferty D., 2015, Astrophys. Source Code Libr.

Moore D. F., Aguirre J. E., Parsons A. R., Jacobs D. C., Pober J. C., 2013, ApJ, 769, 154

Morales M. F., Bowman J. D., Hewitt J. N., 2006, ApJ, 648, 767

Morales M. F., Hewitt J., 2004, ApJ, 615, 7

Morales M. F., Matejek M., 2009, MNRAS, 400, 1814

Mortlock D., 2016, in Mesinger A., ed., Understanding the Epoch of Cosmic Reionization: Challenges and Progress Vol. 423 of Astrophysics and Space Science Library, Quasars as Probes of Cosmological Reionization. p. 187

Mozdzen T. J., Bowman J. D., Monsalve R. A., Rogers A. E. E., 2017, MNRAS, 464, 4995

Mozdzen T. J., Mahesh N., Monsalve R. A., Rogers A. E. E., Bowman J. D., 2018, MNRAS, p. 3240

Noordam J. E., de Bruyn A. G., 1982, Nat, 299, 597

Nunhokee C. D., 2018, In prep.

Nunhokee C. D., Bernardi G., Kohn S. A., Aguirre J. E., Thyagarajan N., Dillon J. S., Foster G., et al., 2017, ApJ, 848, 47

Ord S. M., Mitchell D. A., Wayth R. B., Greenhill L. J., Bernardi G., Gleadow S., et al., 2010, PASP, 122, 1353

Ouchi M., Shimasaku K., Furusawa H., Saito T., Yoshida M., Akiyama M., Ono Y., et al., 2010, ApJ, 723, 869

Parsons A., Backer D., 2009, AJ, 138, 219

Parsons A. R., Backer D. C., Foster G. S., Wright M. C., Bradley R. F., Gugliucci N. E., Parashare C. R., et al., 2010, AJ, 139, 1468

Parsons A. R., Pober J. C., Aguirre J. E., Carilli C. L., Jacobs D. C., Moore D. F., et al., 2012, ApJ, 756

Patil A. H., Yatawatta S., Zaroubi S., Koopmans L. V. E., de Bruyn A. G., Jelić V., Ciardi B., et al., 2016, MNRAS, 463, 4317

Patra N., Subrahmanyan R., Sethi S., Shankar N. U., Raghunathan A., 2015, The Astrophysical Journal, 801, 138

Pen U.-L., Chang T.-C., Hirata C. M., Peterson J. B., Roy J., Gupta Y., Odegova J., Sigurdson K., 2009, MNRAS, 399, 181

Penzias A. A., Wilson R. W., 1965, ApJ, 142, 419

Perley R. A., Schwab F. R., Bridle A. H., eds, 1989, Synthesis imaging in radio astronomy Vol. 6 of Astronomical Society of the Pacific Conference Series

Pindor B., 2018, Proc. Int. Astron. Union, 12, 83

Planck Collaboration Ade P. A. R., Aghanim N., Arnaud M., Ashdown M., Aumont J., Baccigalupi C., et al., 2016, AAP, 594, A13

Platania P., Burigana C., Maino D., Caserini E., Bersanelli M., Cappellini B., Mennella A., 2003, AAP, 410, 847

Pober J. C., 2015, MNRAS, 447, 1705

Pober J. C., Hazelton B. J., Beardsley A. P., Barry N. A., Martinot Z. E., et al., 2016, ApJ, 819, 0

Pober J. C., Parsons A. R., Aguirre J. E., Ali Z., Bradley R. F., Carilli C. L., DeBoer D., Dexter M., et al., 2013, ApJ, 768, L36

Prandoni I., Gregorini L., Parma P., de Ruiter H. R., Vettolani G., Wieringa M. H., Ekers R. D., 2001, AAP, 365, 392

Price D. C., Greenhill L. J., Fialkov A., Bernardi G., Garsden H., Barsdell B. R., Kocz J., et al., 2018, MNRAS, 478, 4193

Pritchard J. R., Furlanetto S. R., 2007, MNRAS, 376, 1680

Pritchard J. R., Loeb A., 2012, Reports Prog. Phys.

Procopio P., Wayth R. B., Line J., Trott C. M., Intema H. T., Mitchell D. A., Pindor B., et al., 2017, pasa, 34, e033

Reichardt C. L., 2016, in Mesinger A., ed., Understanding the Epoch of Cosmic Reionization: Challenges and Progress Vol. 423 of Astrophysics and Space Science Library, Observing the Epoch of Reionization with the Cosmic Microwave Background. p. 227

Rengelink R. B., Tang Y., de Bruyn A. G., Miley G. K., Bremer M. N., Röttgering H. J., Bremer M. A., 1997, Astron. Astrophys. Suppl. Ser., 124, 259

Rogers A. E. E., Bowman J. D., 2008, AJ, 136, 641

Rybicki G. B., Lightman A. P., 1986, Radiative Processes in Astrophysics. Wiley-VCH

Ryden B., 2013, Introduction to Cosmology. Always Learning, Pearson Education

Santos M. G., Amblard A., Pritchard J., Trac H., Cen R., Cooray A., 2008, ApJ, 689, 1

Santos M. G., Cooray A., Knox L., 2005, ApJ, 625, 575

Sault R., Conway J., 1999, in Taylor G., Carilli C., Perley R., eds, Synth. Imaging Radio Astron. II Vol. 180 of Astronomical Society of the Pacific Conference Series, Multi-Frequency Synthesis. p. 419

Schwab F. R., 1984, in Roberts J. A., ed., Indirect Imaging. Measurement and Processing for Indirect Imaging Optimal Gridding of Visibility Data in Radio Interferometry. pp 333–346

Shaver P. A., Windhorst R. A., Madau P., de Bruyn A. G., 1999, AAP, 345, 380

Smirnov O. M., 2011a, AAP, 527, A106

Smirnov O. M., 2011b, AAP, 527, A107

Sullivan I. S., Morales M. F., Hazelton B. J., Arcus W., Barnes D., 2012, ApJ, 759, 2

Tasse C., van der Tol, S. van Zwieten, J. van Diepen, G. Bhatnagar, S. 2013, A&A, 553, A105

Taylor G., Carilli C., Perley R., eds, 1999, Synthesis Imaging in Radio Astronomy II Vol. 180 of Astronomical Society of the Pacific Conference Series. Astronomical Society of the Pacific Conference Series

Thompson A. R., Moran J. M., Swenson G. W., 2017, Interferometry and Synthesis in Radio Astronomy. Springer International Publishing, Cham, pp 89–108

Tingay S. J., Goeke R., Bowman J. D., Emrich D., Ord S. M., 2013, Publ. Astron. Soc. Aust., 30

Treu T., Schmidt K. B., Trenti M., Bradley L. D., Stiavelli M., 2013, The Astrophysical Journal Letters, 775, L29

Van de Hulst H., 1945, Ned. Tijdschr. Natuurk, 11, Pages={210

van Haarlem M. P., Wise M. W., Gunst A. W., Heald G., McKean J. P., et al., 2013, A&A, 556, A2

Wang X., Tegmark M., Santos M., Knox L., et al., 2006, ApJ, 650, 529

Wieringa M. H., de Bruyn A. G., Jansen D., Brouw W. N., Katgert P., 1993, AAp, 268, 215

Wouthuysen S. A., 1952, AJ, 57, 31

Yatawatta S., de Bruyn A. G., Brentjens M. A., Labropoulos P., Pandey V. N., Kazemi S., Zaroubi S., et al., 2013, AAP, 550, A136

Zahn O., Reichardt C. L., Shaw L., Lidz A., Aird K. A., Benson B. A., et al., 2012, ApJ, 756, 65

Zaldarriaga M., 1997, Phys. Rev. Lett., 55, 1820

Zaroubi S., 2013, in Wiklind T., Mobasher B., Bromm V., eds, The First Galaxies Vol. 396 of Astrophysics and Space Science Library, The Epoch of Reionization. p. 45

Zheng H., Tegmark M., Buza V., Dillon J. S., Gharibyan H., Hickish J., Kunz E., Liu A., et al., 2014, MNRAS, 445, 1084